Title

Promotion of particle formation by resonance-stabilized radicals during hydrocarbon pyrolysis

Authors

Rundel, James A

Thomas, Charlotte M

Schrader, Paul E

et al.

Publication Date

2022-09-01

DOI

10.1016/j.combustflame.2021.111942

Combustion and Flame 243 (2022) 111942

Contents lists available at ScienceDirect

Combustion and Flame

journal homepage: www.elsevier.com/locate/combustflame

Promotion of particle formation by resonance-stabilized radicals during hydrocarbon pyrolysis

James A. Rundel[a], Charlotte M. Thomas[a], Paul E. Schrader[b], Kevin R. Wilson[c], K. Olof Johansson[b,d], Ray P. Bambha[b], Hope A. Michelsen[a,b,e,*]

[a] Department of Mechanical Engineering, University of Colorado Boulder, 1111 Engineering Drive, Boulder, CO 80309 USA
[b] Combustion Research Facility, Sandia National Laboratories, P. O. Box 969, MS 9055, Livermore, CA 94551 USA
[c] Chemical Sciences Division, Lawrence Berkeley National Laboratory, Berkeley, CA 94720 USA
[d] Presently at KLA Corporation, Milpitas, CA 95035 USA
[e] Environmental Engineering Program, University of Colorado Boulder, 1111 Engineering Drive, Boulder, CO 80309 USA

ARTICLE INFO

Article history:
Received 17 October 2021
Revised 11 December 2021
Accepted 12 December 2021
Available online 29 December 2021

Keywords:
Pyrolysis
Ethylene
Indene
Resonance-stabilized radicals
Soot
Inception

ABSTRACT

We measured aerosol mass spectra and mobility size distributions of particles formed during the pyrolysis of ethylene, indene, and a mixture of ethylene with a small amount of indene. Measurements were recorded with a scanning mobility particle sizer and an aerosol mass spectrometer employing vacuum ultraviolet photoionization using tunable radiation from the Advanced Light Source at Lawrence Berkeley National Laboratory. The results demonstrate that particle formation occurs at a temperature of ~1123±50 K for ethylene alone, at ~923±50 K for indene alone, and at a comparable temperature to that of indene for ethylene seeded with a small amount of indene. Our results demonstrate that indene and indenyl, a resonance-stabilized radical (RSR) formed from indene pyrolysis, promote particle formation at lower temperatures and in the absence of acetylene, supporting the hypothesis that RSRs promote soot-particle inception. Even a small amount of indene added to ethylene promotes particle formation while circumventing the traditional pathways for mass growth by acetylene-addition reactions. Further support is provided by the appearance in the aerosol mass spectra of prominent peaks for masses corresponding to other RSRs from particles formed at lower pyrolysis temperatures. In addition, odd-numbered carbon species, associated with RSRs, appear in higher concentrations at low temperatures and are closely tied to particle inception. In indene pyrolysis, mass signals indicative of covalently bound indenyl dimers and trimers are prominent at pyrolysis temperatures near soot onset. Photoionization efficiency (PIE) curves demonstrate that, while the isomeric composition for some of these peaks may differ between ethylene and indene, the addition of indene to ethylene does not notably alter the isomers formed at these peaks between ethylene and the ethylene-indene mixture. PIE curves also show that *m/z* 202, which is commonly assumed to be pyrene, is composed principally of fluoranthene under these conditions.

1. Introduction

Soot plays a significant role in global human health and the environment. Combustion-generated particles are especially harmful to human health compared to similar particles that are not a byproduct of combustion processes [1]. These particles are linked to a wide array of detrimental health effects, including lung disease and altered cardiac function [2]. Soot particles also incorporate polycyclic aromatic hydrocarbons (PAHs), some of which have been labeled as priority pollutants by the U.S. EPA and are known carcinogens [3]. Research into the scope and severity of health effects caused by these particles is ongoing, but soot emissions are estimated to be responsible for millions of deaths annually [2, 4, 5]. In addition to health impacts, soot absorbs strongly throughout the ultraviolet, visible, and infrared spectral regions and is a significant contributor to climate change, primarily through enhanced direct radiative forcing [6, 7]. These particles also have secondary radiative effects related to decreasing surface albedo following deposition on snow and ice and serving as atmospheric cloud nucleation sites [6, 7]. These particles have thus become subject to increasingly stringent regulations, and interest in mitigation strategies has grown.

* Corresponding author.
E-mail address: hope.michelsen@colorado.edu (H.A. Michelsen).

https://doi.org/10.1016/j.combustflame.2021.111942

A robust understanding of the chemistry and mechanisms involved in the formation of soot particles is critical for accurately modeling and predicting soot-formation rates and physicochemical properties. Accurate representations of these processes could lead to improved control or mitigation strategies. A sizeable body of research has developed around experimental studies of soot particles and precursors and modeling of precursor kinetics, particle growth, and soot yield. Nevertheless, mechanisms for precursor growth and particle production are poorly understood.

The largest and most widely accepted class of soot precursors is PAHs, which have long been linked to soot formation and are generally assumed to act as the building blocks of soot particles [8–12]. Despite widespread acceptance that PAHs play a significant role in soot formation, the mechanisms explaining precursor growth and particle inception are still debated. There has been extensive research into the gas-phase development of PAHs using chemical kinetic models. Wang and Frenklach [13, 14] initially proposed the hydrogen abstraction C_2H_2 addition (HACA) mechanism as a method for precursor growth via acetylene addition, and it has been repeatedly supported by experimental and theoretical evidence [15–20]. HACA does not accurately capture the rate of particle growth [21, 22], however, and is too distributed to explain particle inception [23], i.e., the transition from the gas phase to the condensed phase [24]. Models of soot formation and growth tend to be empirical or semi-empirical because of the wide range of chemical species, time scales, and spatial scales involved. For example, many kinetic models invoke physical dimerization of smaller PAHs, such as pyrene, as a proxy for soot inception, despite strong theoretical and experimental evidence against small-PAH dimerization by van der Waals forces [21, 25-29].

Two broad and overlapping classes of mechanisms for particle inception are currently under active consideration. On one end of the spectrum of mechanisms are those mechanisms predominantly driven by the thermodynamic processes of nucleation and condensation, and on the other end are mechanisms controlled by chemical kinetic rates and probabilities of reaction. Particles formed during thermodynamically driven inception are thought to be formed of stacked PAHs held together by van der Waals forces [21, 30, 31]. This mechanism class is challenged by experimental and theoretical evidence demonstrating that the PAHs typically observed during soot inception are too small to condense at flame temperatures [21, 26, 28]. During kinetically controlled inception, precursors cluster through covalent bonding and may form clusters of cross-linked aromatic species [23, 32-35]. Kinetically controlled mechanisms are generally constrained by high reaction barriers and slow reaction rates for relevant reactions. Such mechanisms often involve schemes predicting the activation or dimerization of stable PAHs, which results in particle formation at slower rates than experimentally observed [14, 21]. Radical-based reactions have long been posited as a pathway for faster precursor growth [36–40]. A recent study by Johansson et al. [23] proposed a mechanism, clustering of hydrocarbons through radical-chain reactions (CHRCR), in which resonance-stabilized radicals participate in hydrocarbon clustering via radical-chain reactions, providing an efficient route for particle inception and growth.

Previous pyrolysis studies of ethylene and indene have largely focused on the analysis of gas-phase products smaller than pyrene [16, 17, 41] and analysis of soot particles and condensate using GC–MS, light scattering, or mobility analysis [42–47]. Recent studies by Jin et al. [48, 49] provide a detailed investigation of gas-phase products associated with indene pyrolysis and relevant improvements to kinetic mechanisms. The current work builds on previous studies by using aerosol mass spectrometry (AMS) coupled with tunable vacuum-ultraviolet (VUV) radiation for online investigations of soot and particle-associated products over a wider mass range. The aim of this study is to explore the influence of resonance-stabilized radicals (RSRs) on precursor formation and particle inception in ethylene and indene pyrolysis. Photoionization efficiency (PIE) curves are also used to investigate the isomeric composition of selected peaks. We observed that the presence of small amounts of indene in ethylene pyrolysis promotes particle inception by providing a larger RSR pool, thus supporting the hypothesis put forward by Johansson et al. [23].

2. Experimental and analysis methods

2.1. Experimental setup

Experiments were performed at Beamline 9.0.2, the Chemical Dynamics Beamline, at the Advanced Light Source (ALS) synchrotron facility at Lawrence Berkeley National Laboratory in Berkeley, CA. The experimental setup consists of a laminar flow reactor and a time-of-flight aerosol mass spectrometer using synchrotron tunable vacuum ultraviolet photoionization (VUV-AMS) [50, 51]. The laminar flow reactor is made of a quartz tube with a total length of 58.4 cm and an inner diameter of 1.08 cm. The heated length of the reactor is 40.6 cm, and the reactor was heated using an electric furnace (MHI-H17HTC). The pressure in the reactor was approximately 1 atm. All gas flow rates were controlled using mass flow controllers (MKS Instruments, Inc. Model GM50A) with flow stability of ±3% at full scale, calibrated (using a Sierra Instruments, Inc. Model SL-500) prior to use. Research-grade gasses were supplied by Airgas, Inc. and were filtered (Swagelok Model SS-4F-05) immediately upstream of the mass flow controllers. Flow rates are given in standard (0 °C, 1 atm) cubic centimeters per minute (sccm).

Soot particles were generated through the pyrolysis of indene (C_9H_8), ethylene (C_2H_4), and an ethylene-indene mixture at temperatures between 873 K and 1573 K. For ethylene pyrolysis, a flow of 5 sccm ethylene and 200 sccm argon was supplied to the reactor inlet. For indene pyrolysis, 50 sccm of argon was bubbled through a U-tube containing liquid indene maintained at 296 K, resulting in an indene vapor flowrate of approximately 0.1 sccm. The indene-saturated argon flow was diluted with an additional 200 sccm of argon before entering the reactor. For the ethylene-indene mixture, 5 sccm ethylene was seeded with 0.1 sccm indene and diluted with 250 sccm argon. We estimated the residence times at 973 K to be 3.06 s for ethylene, 2.51 s for indene, and 2.46 s for the ethylene-indene mixture.

After exiting the reactor, the products were quenched with a 3000 sccm flow of nitrogen (N_2), and a continuous sample was directed into the VUV-AMS. The VUV-AMS includes an aerodynamic lens (ADL) system [52–54], which removes small particles and gas-phase species and focuses particles larger than ~50 nm into a beam. The transmission function and other characteristics of the ADL system and particle beam have been described previously [52–54]. In our experiment small particles tend to coagulate in the sampling line and are transmitted to the detection region despite being below the transmission limit of the ADL system when formed. The particle beam is focused onto a copper target in a vacuum chamber with a working pressure of 10^{-6} Torr. The target is heated to approximately 623 K to vaporize condensed and weakly bound species from the particles. These vaporized species are photoionized with VUV radiation, pulse-extracted at a rate of 15 kHz, and analyzed with time-of-flight mass spectrometry. All mass spectra shown were recorded with a photon energy of 9.5 eV to ionize products.

The relationship between VUV-AMS signal and species concentrations is difficult to quantify; the VUV-AMS measures species that adsorb onto soot particles strongly enough to remain attached to the particle during transit to the ionization chamber but weakly enough to vaporize from the heated copper target under vacuum.

These species do not necessarily reproduce a representative concentration distribution of the species that are present in the pyrolysis products. This behavior has previously been noted to concentrate certain radicals and demonstrate greater sensitivity to heavier masses (i.e., $m/z > \sim 190$), despite the lower concentrations of these larger species [23].

The VUV soft photoionization limits species fragmentation. The species are assumed to be singly ionized. However, the photon-energy distribution of the VUV radiation is relatively broad, with a spread of approximately 0.2 eV fullwidth at half maximum. A small amount of 2,5-dimethylfuran was bled into the ionization chamber to serve as a mass marker for time-of-flight calibration and as a reference for photon flux. A reference for the photon flux was needed to determine relative photoionization cross-sections, and 2,5-dimethylfuran was selected based on favorable characteristics identified in previous experiments [55].

We also made measurements of mobility size distributions of soot particles produced during ethylene and indene pyrolysis. In these experiments, ethylene and indene were pyrolyzed using the same conditions as given above, but argon was replaced with nitrogen as the bath gas. At the exit of the reactor, the products were quenched with an additional 3000 sccm flow of nitrogen, and particles were analyzed using a scanning mobility particle sizier (SMPS, electrostatic classifier Model 3080, differential mobility analyzer, Model 3081, condensation particle counter, Model 3776, TSI, Inc.). For these measurements, we used a differential mobility analyzer (DMA) capable of measuring particle size distributions and average particle mobility sizes within the range of ~10 – 600 nm.

2.2. Analysis

Peak intensities for a given m/z are expressed as the integrated area under a peak. The integrated area for a peak was calculated by fitting the peak to the functional form of a gaussian or exponentially modified gaussian distribution and subtracting the baseline, which was fit using the LogPoly5 baseline function in Igor Pro (Version 8.04, WaveMetrics [56]). All mass spectra are scaled to the peak with the highest intensity, excluding m/z 96, which corresponds to the 2,5-dimethylfuran added in the ionization chamber.

Photoionization efficiency (PIE) curves, which represent the dependence of ion intensity for a given mass peak on photon energy, were obtained by scanning photon energy between 7.5 - 10.2 eV in 0.1 eV increments. We convolved the photon energy distribution at 9.0 eV with the photoionization cross-section of 2,5-dimethylfuran published by Xie et al. [57] to create a reference curve for 2,5-dimethylfuran. The PIE curves for pyrolysis products were normalized by the intensity of the dimethylfuran peak and scaled by the reference curve for 2,5-dimethylfuran to account for photon flux. For consistency between experimental sets and fuel types, the corrected PIE curves for pyrolysis products were arbitrarily normalized by the signal at 10.2 eV. To compare PIE curves between fuels, a fit between two curves was performed using two parameters: a scaling factor and an offset. We made comparisons between PIE curves for pyrolysis products and reference PIE curves taken from the literature. We performed a two-parameter fit in which we convolved the reference curves with the photon-energy distribution and then applied scaling factors and an offset parameter. We assumed a linear combination of the reference curves during the fitting procedure in comparisons involving multiple reference curves. Reference curves for selected species were drawn from the literature. A complete list of species for which comparisons were made can be found in Section A of the supplementary material. In addition, we have included a species dictionary with possible species structures in Section B of the supplementary material.

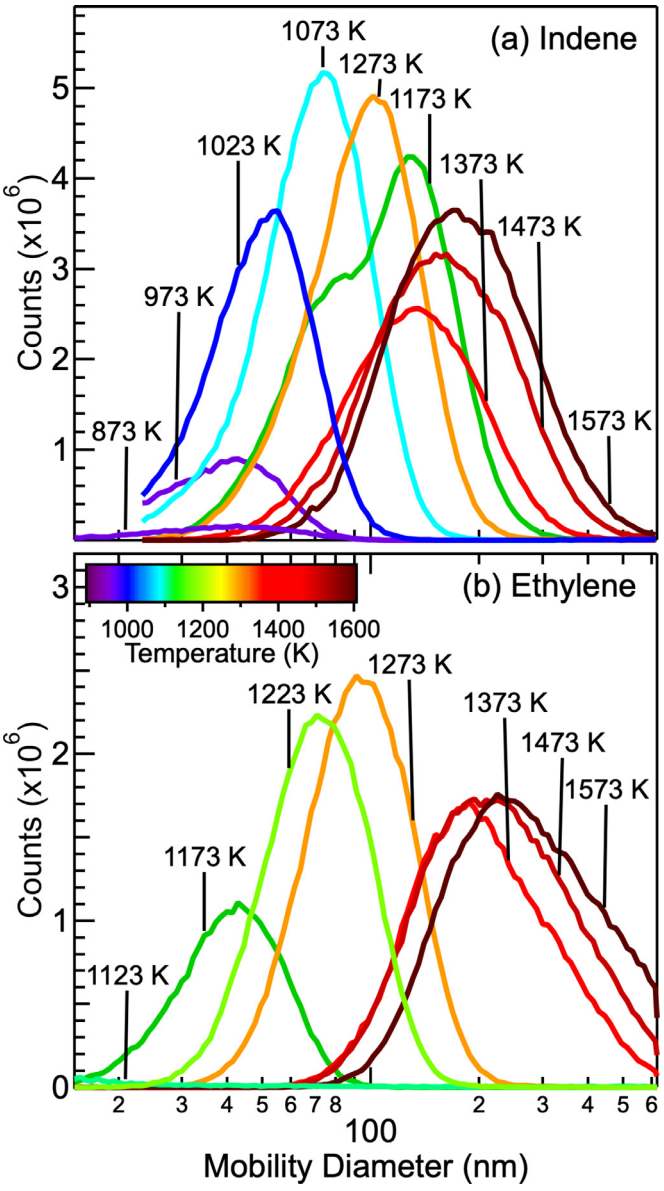

Fig. 1. Temperature dependence of particle size distributions. SMPS size distributions are shown for (a) indene and (b) ethylene as a function of the pyrolysis flow-reactor temperature, color-coded and labeled by temperature. Color coding for both (a) and (b) is shown in the color bar in (b).

3. Results and discussion

3.1. Particle-formation temperatures

Fig. 1 shows the temperature dependence of size distributions of particles formed during pyrolysis. The SMPS size distributions demonstrate that particles start to form at ~923±50 K for indene and ~1123±50 K for ethylene. The average particle sizes are summarized in Fig. 2a for indene and Fig. 2b for ethylene. Particles are observed at much lower temperatures for indene pyrolysis than for ethylene pyrolysis.

The size distributions shown in Fig. 1 demonstrate a general increase in particle size with increasing temperature. At 1173 K, the size distributions for indene pyrolysis are bimodal. This temperature is close to the temperature at which Jin et al. [49] reported that indene decomposes and forms acetylene at 760 Torr, and we speculate that this second larger mode represents the availability

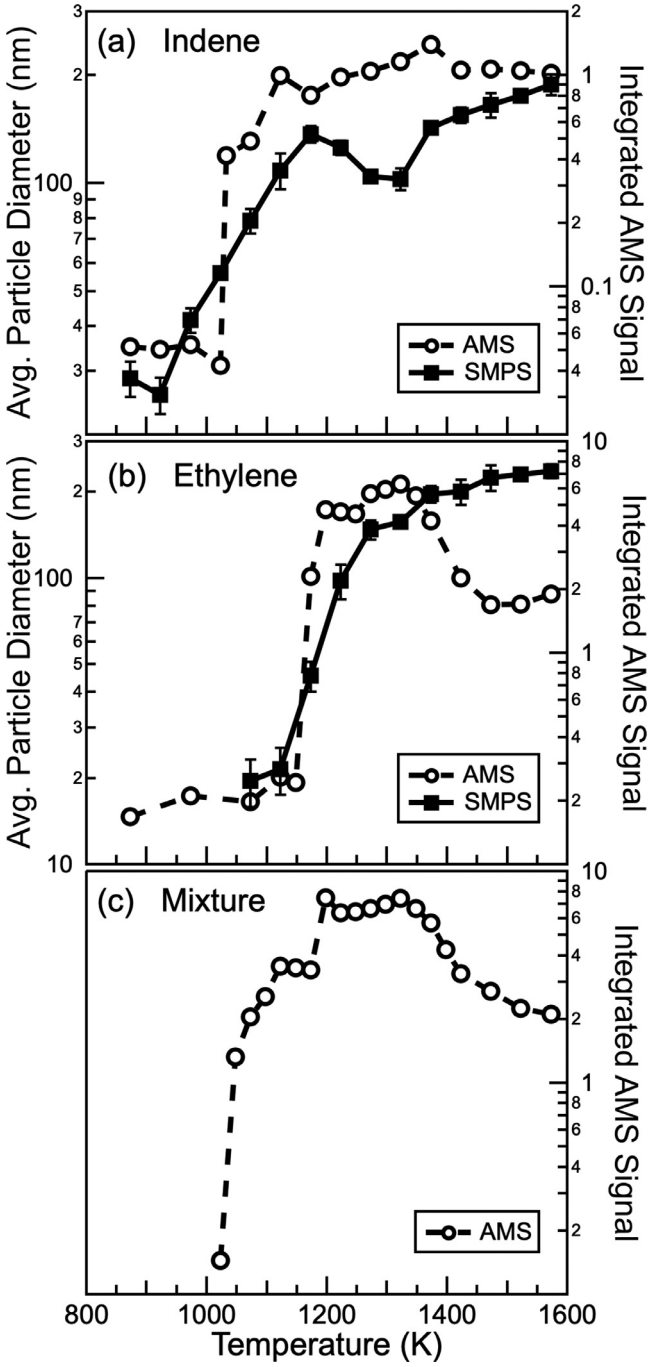

Fig. 2. Temperature dependence of particle formation. Integrated ion counts for VUV-AMS signal (dashed lines, open symbols), and average particle size measured by SMPS (solid lines and symbols) are shown as a function of the pyrolysis flow-reactor temperature. Data are shown for (a) indene, (b) ethylene, and (c) the ethylene-indene mixture. Error bars represent the standard deviation of experimental trials.

of additional pathways for particle growth, potentially involving traditional HACA pathways. It appears that the second mode then begins to grow with increasing temperature. This second mode appears at sizes of ~100 nm, which is larger than the first mode, suggesting that this second mode is not a result of new pathways for inception. This observation is consistent with the hypothesis that indenyl-driven reactions are responsible for particle inception at lower temperatures. As indenyl decomposes at higher temperature, it is no longer available to promote particle formation and growth whereas species such as acetylene become available.

Fig. 2 shows comparisons of the SMPS mean particle sizes with the integrated ion counts from the VUV-AMS as a function of temperature. The VUV-AMS produces signal when particles of sufficient size (>~50 nm) are formed or coagulate in the sampling line. Because of the limited transmission at the smallest particle sizes, these measurements tend to demonstrate a higher particle onset temperature than do SMPS measurements. This effect is demonstrated in Fig. 2a by the appearance of particles at a lower temperature in SMPS measurements than suggested by the VUV-AMS signal. Nevertheless, the VUV-AMS data provide a point of comparison, across fuels, for when particles grow to sizes large enough to produce discernible signal in the VUV-AMS.

The integrated VUV-AMS signal indicates that soot onset occurs between 1023 and 1033 K for indene, between 1148 and 1173 K for ethylene, and between 1023 and 1048 K when we add a small amount of indene (~2% by number density) to the ethylene, as shown in Fig. 2. The onset temperature observed when a small amount of indene is added to ethylene is significantly lower than that observed for ethylene alone. Given the temperature resolution of the experiments, the ethylene-indene mixture begins to form particles within the same temperature range as indene. The comparable onset temperatures between the ethylene-indene mixture and pure indene suggest that particle inception and growth in the mixture is driven by indene-initiated reactions. Indene is a precursor for RSR formation and forms indenyl during pyrolysis; the reduction in the particle onset temperature with the addition of this RSR precursor provides strong evidence that RSR reactions are important in driving particle formation at temperatures near 1000 K.

3.2. Ethylene pyrolysis

Past experimental studies of ethylene pyrolysis examined gas-phase [17, 58] and condensed-phase or particle-associated products [16, 41, 44, 45]. These studies focused primarily on initial decomposition products and closed-shell aromatic species with $m/z <$ ~300. Mass spectra obtained via VUV-AMS (Fig. 3) show a broader and more detailed distribution of products, including radicals, than observed previously.

There are a large number of peaks in the mass spectrum at the particle threshold temperature for ethylene pyrolysis (Fig. 3b). The abundance and rapid development of peaks indicate that multiple pathways, such as HACA and radical-radical reactions [23, 37, 59, 60], contribute to precursor growth. These peaks appear in clusters, separated by approximately the mass of a carbon atom, i.e., 12 u. At high temperatures (e.g., Fig. 3a), peak clusters associated with an even number of carbon atoms tend to be larger than those associated with an odd number of carbon atoms. As noted below, however, this trend switches at lower temperatures close to the onset of particle formation (Fig. 3b). Peak series for both odd and even numbers of carbon atoms are separated by 24 u or 26 u, as others have previously noted in examinations of gas-phase species [17, 58, 61]. A sequence of radical peaks, previously hypothesized to be linked to resonance-stabilized radicals (RSRs) by Johansson et al. [23], is also apparent and denoted in Fig. 3. These RSR masses are associated with odd-numbered carbon sets and are one mass unit lower than the primary closed-shell peak in the odd-carbon series. This observation is consistent with the association between RSRs, five-membered-ring structures, and odd-carbon numbers [23]. Conversely, the dominant peaks of the even-numbered carbon series are not typically coupled with radical masses in the mass spectra.

The RSR masses follow the same spacing of 24–24–26 u as the major peaks, and the sequence extends through the end of the observable peak series. At 1173 K, when particles are first de-

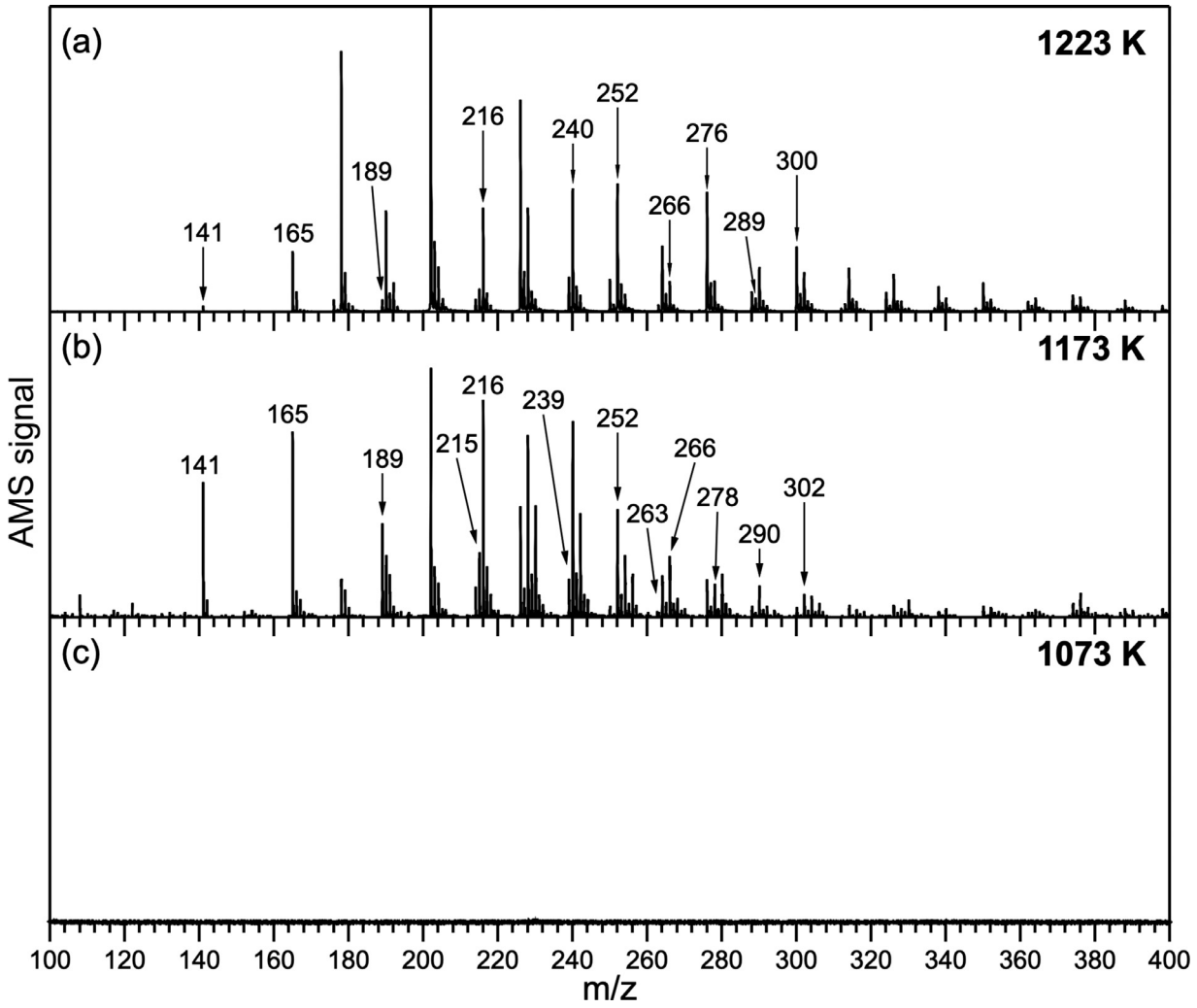

Fig. 3. VUV-AMS mass spectra of ethylene pyrolysis products. Results are shown for flow-reactor temperatures of (a) 1223 K, (b) 1173 K, and (c) 1073 K. The data were recorded with a photon energy of 9.5 eV. Major peaks and masses corresponding to proposed resonance-stabilized radicals and relevant closed-shell species are labeled.

tected, the mass spectra show unexpectedly high signals for peaks corresponding to odd-numbered carbon species and RSRs. Specifically, peaks for radical masses at *m/z* 141 ($C_{11}H_9$), 165 ($C_{13}H_9$), and 189 ($C_{15}H_9$) are larger than the corresponding closed-shell peaks. Above *m/z* 189, the radical masses are apparent, but the associated closed-shell peaks at *m/z* 216 ($C_{17}H_{12}$), 240 ($C_{19}H_{12}$), and 264 ($C_{21}H_{12}$) are present at higher intensities than their radical partners. This trend may indicate that, at lower masses, radicals have a higher affinity for the particles than do closed-shell species, and that the adsorption probability increases for closed-shell species with increasing mass. This trend also suggests that these RSRs and odd-numbered carbon species may be relatively abundant and play a significant role in particle inception.

3.3. Indene pyrolysis

For indene pyrolysis, particle formation occurs at temperatures lower than that at which acetylene is formed through indene pyrolysis (1200 K at 760 Torr [49]); particles are thus formed in the absence of acetylene, which demonstrates particle formation without the involvement of traditional HACA pathways. This conclusion is consistent with early work in shock tubes by Graham et al. [43] that showed that, under their pyrolysis conditions, indene formed soot more readily than acetylene and without involving the decomposition of indene.

In contrast to ethylene pyrolysis products, there is a relatively sparse set of mass peaks observed for indene pyrolysis, as shown in Fig. 4, even at higher temperatures. The initial sparsity in peaks may be due, in part, to the stability of the indenyl radical, which impedes decomposition routes for indene [49]. Given the availability and stability of indenyl during the initial decomposition process, species growth via indenyl-based reactions is favored over continued decomposition at lower temperatures. This propensity for species growth from reactions with indenyl is demonstrated in Fig. 4. At 1073 K (~40 K above sooting onset as measured by VUV-AMS), major peaks include *m/z* 216 ($C_{17}H_{12}$), 228 ($C_{18}H_{12}$), and 230 ($C_{18}H_{14}$). Previous studies on indene pyrolysis have also demonstrated these masses as major products and proposed reaction pathways to both C_{17} and C_{18} products based on indenyl reactions [48, 49, 62]. Lu and Mulholland [62] calculated reaction pathways, summarized in Scheme 1, for which a bi-indenyl structure can undergo a series of ring-closing and opening steps to form isomers of *m/z* 228, chrysene, benzo[*c*]phenanthrene, and benz[*a*]anthracene. Such pathways were also proposed by Badger and Kimber [63, 64] and Wentrup et al. [65]. The formation of chrysene from indenyl dimer formation was also proposed in 1966 by Davies and Scully [42]. Lu and Mulholland [62] additionally proposed a pathway for formation of benzo[*b*]fluorene (*m/z* 216), a C_{17} product, via loss of the methyl group from the proposed intermediate methyl benzo[*b*]fluorene, as shown in Scheme 2. Jin et al. [48,

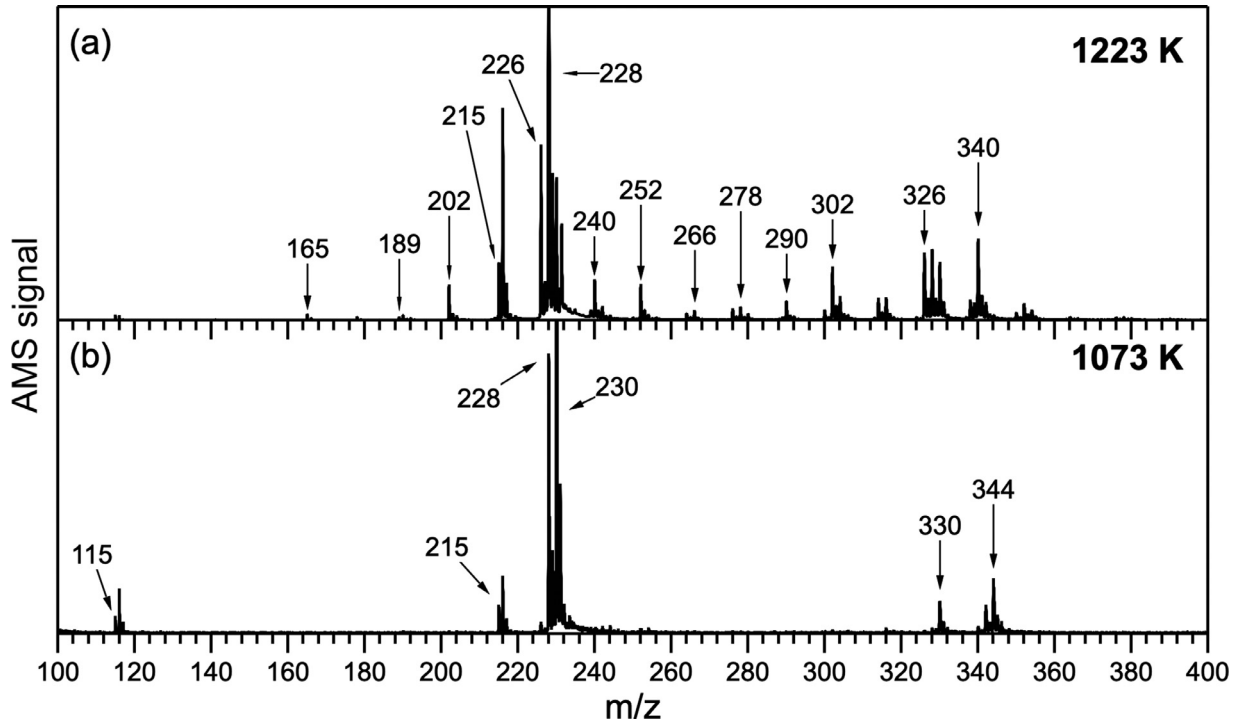

Fig. 4. VUV-AMS mass spectra of indene pyrolysis products. Results are shown for reactor temperatures of (a) 1223 K and (b) 1073 K. The data were recorded with a photon energy of 9.5 eV. Major peaks and masses corresponding to proposed resonance-stabilized radicals and relevant closed-shell species are labeled.

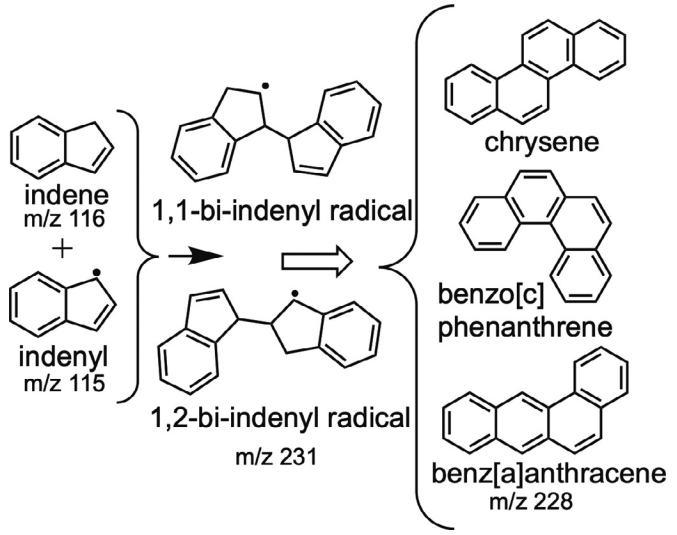

Scheme 1. Summary of indenyl dimerization and subsequent isomerization pathways proposed by Badger and coworkers [63, 64], Lu and Mullholland [62], and Wentrup et al. [65] to form isomers at *m/z* 228. Solid arrows represent single-step reactions, and hollow arrows represent multi-step reactions. Chrysene formation was also proposed by Davies and Scully [42].

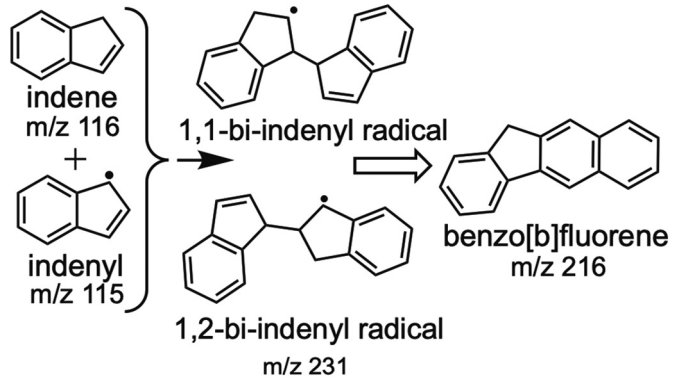

Scheme 2. Indenyl dimerization and isomerization pathway to form C_{17} species. This scheme is based on pathways proposed by Lu and Mullholland [62] and by Jin et al. [48, 49], based on an analogous scheme from Kislov and Mebel [66]. Solid arrows represent single-step reactions, and hollow arrows represent multi-step reactions.

49] proposed a route to the formation of benzo[*b*]fluorene via the bi-indenyl radical (Scheme 2); their pathway proceeds via methyl benzo[*b*]fluorenyl and is based on the scheme for indene formation via the cyclopentadiene-cyclopentadienyl adduct proposed by Kislov and Mebel [66].

Whereas bi-indenyl is the dominant route to forming $C_{18}H_{14}$, other pathways may exist after further decomposition of indene, such as the radical-radical combination of fluorenyl ($C_{13}H_9$) and cyclopentadienyl (C_5H_5) [48, 62, 65]. These reaction schemes emphasize the importance and involvement of radical-radical reactions and resonance-stabilized radicals in precursor growth. The importance of these types of reactions has been previously noted [40, 59, 67] and is consistent with the CHRCR mechanism.

In addition to peaks at *m/z* 216, 228, and 230, prominent peak sets observed include *m/z* 330 ($C_{26}H_{18}$) and 344 ($C_{27}H_{20}$), beginning at 1033 K when particles are first detected in the VUV-AMS mass spectra. These masses were not observed in gas phase studies of indene pyrolysis [48, 49, 60, 62, 65]. The combinations of observed masses and the initial sparsity of peaks in the mass spectra suggest that these peak series are formed from reactions of indenyl with C_{17} and C_{18} species. The stability of the C_{26} and C_{27} species throughout the vaporization and ionization processes indicates that they are covalently bound and not physical dimers. The presence of the mass peaks at *m/z* 330 and 344 among the first masses detected by the VUV-AMS indicates that these species

may be rapidly and efficiently formed through radical-clustering-type reactions, such as those predicted by the CHRCR mechanism.

As reactor temperature increases between 1073 and 1223 K, the major peaks in the C_{26} and C_{27} series shift downward by 2–4 mass units. In this temperature range, very few peak series are observed between *m/z* 230 and 330, and this downward shift corresponds to a similar shift in intensities for the C_{18} series. These trends imply a direct link between these masses that is indicative of growth through repeated indenyl addition.

There are fewer RSR mass peaks in indene pyrolysis across all temperatures, relative to the number observed in ethylene pyrolysis. The sparsity of RSR peaks is likely attributable to the lack of acetylene or vinyl radical necessary to form the radical pool [23]. Based on previous work [23], we would expect indenyl radical to readily form species with *m/z* of 141 ($C_{11}H_9$), 165 ($C_{13}H_9$), 189 ($C_{15}H_9$), 215 ($C_{17}H_{11}$), 239 ($C_{19}H_{11}$), and 263 ($C_{21}H_{11}$) in the presence of acetylene or vinyl radical. Except for *m/z* 215, these masses are not apparent in the mass spectra associated with lower reactor temperatures. At higher temperatures, however, these masses do appear, suggesting that indene dissociates at these temperatures to form species (i.e., acetylene or vinyl) that can react with indenyl to generate these larger RSRs. This observation is consistent with the results of Jin et al. [49], which demonstrate formation of acetylene in the pyrolysis of indene at temperatures above 1200 K at 760 Torr. Reactions of indenyl with acetylene and vinylacetylene are proposed to form species, such as a vinylindenyl and benzotropyl radical at *m/z* 141 and fluorenyl, phenalenyl, and benz[*e*]indenyl at *m/z* 165 [23, 60], as shown in Scheme 3. Despite calculations suggesting that the production of benzotropyl should be kinetically and thermodynamically favored over that of vinylindenyl in reactions of acetylene with indenyl [60] (Scheme 3a), detailed experiments by Zhao et al. [60] demonstrated that 1-ethynylindene (*m/z* 140) is exclusively formed via the vinylindenyl intermediate at high temperatures and that benzotropyl is not formed (Scheme 3a). At such temperatures we observe only *m/z* 141 and not 1-ethynylindene. We also observe *m/z* 142, which could be produced by hydrogen addition to vinylindenyl to generate the closed-shell species vinylindene (Scheme 3a). Although we cannot rule out production of benzotropyl, our current results and those of Zhao et al. [60] are consistent with the previous identification of *m/z* 141 as vinylindenyl.

3.4. Ethylene-indene mixture pyrolysis

Fig. 5 shows mass spectra for the mixture at several temperatures. Fig. 5c presents the mass spectrum recorded for the pyrolysis temperature of 1073 K, which is above the particle onset temperature for indene and the mixture, but below the onset temperature for ethylene. Fig. 6a shows a comparison of the three fuels for 1073 K. At this temperature, prominent peaks at *m/z* 178 ($C_{14}H_{10}$) and 202 ($C_{16}H_{10}$) are present in the mass spectrum for the mixture that are not observed in indene alone. The presence of these features confirms that reactions at this onset temperature do not involve the pyrolysis products of indene alone, but that the presence of indene/indenyl has a synergistic effect on particle formation through reactions involving ethylene or products from ethylene pyrolysis. The constructive effect of an additional pool of RSRs on particle formation and growth is consistent with behavior predicted by the CHRCR mechanism. Despite the additional features in the mass spectrum for the ethylene-indene mixture, there is a relative sparsity of mass peaks, as with indene pyrolysis. If the HACA mechanism were responsible for the growth in gas-phase precursors associated with particle inception at these temperatures, the VUV-AMS mass spectra would demonstrate a sequence of mass peaks separated in mass by 24 or 26 u. Such a sequence is not apparent in the VUV-AMS mass spectra at temperatures close to

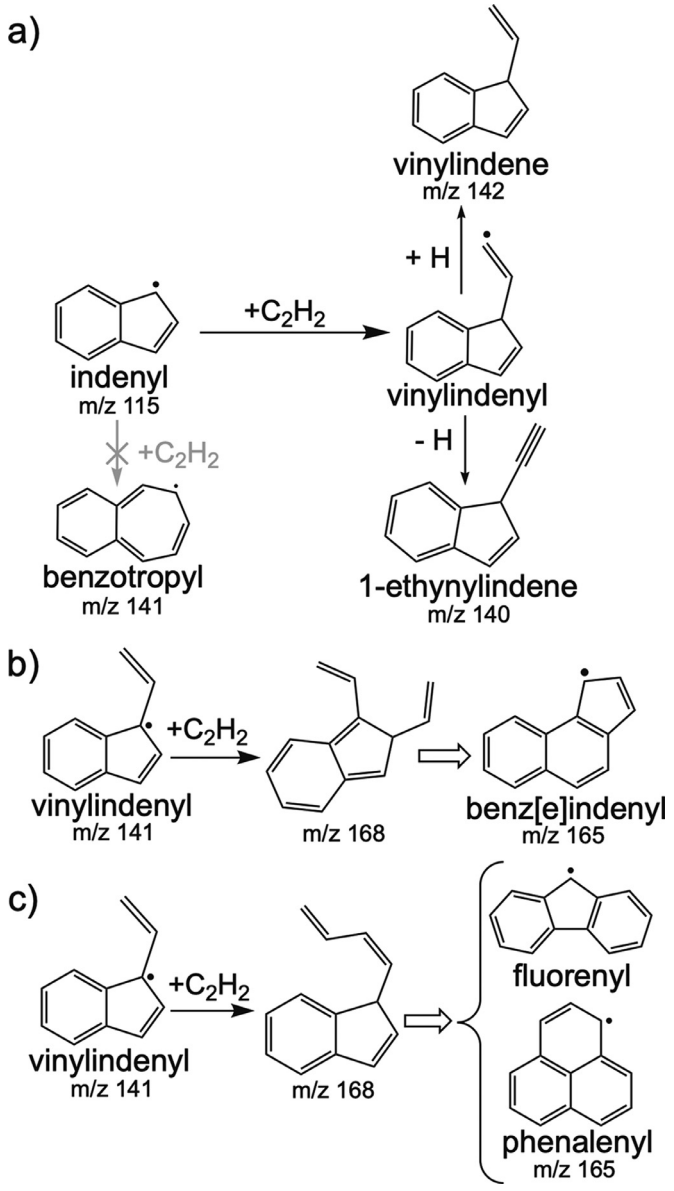

Scheme 3. Summary of acetylene addition to indenyl. Larger RSRs are proposed to form in the reaction of acetylene with indenyl, including vinylindenyl radical (*m/z* 141), benzotropyl radical (*m/z* 141), fluorenyl (*m/z* 165), phenalenyl (*m/z* 165), and benz[*e*]indenyl (*m/z* 165). (a) The first step (1-indenyl to vinylindenyl) was proposed by Johansson et al. [23]. The other steps were proposed by Zhao et al. [60]. (b) – (c) These mechanisms were proposed by Johansson et al. [23]. Solid arrows represent single-step reactions, and hollow arrows represent multi-step reactions.

that of particle onset for either indene or the ethylene-indene mixture. Fig. 5b shows the mass spectrum for 1148 K. At this temperature there are a few additional peaks, largely associated with RSR species. Fig. 6b shows a comparison with ethylene and indene at 1173 K, demonstrating the relative sparsity of peaks in the mixture compared with ethylene alone near the onset temperature for particle formation from ethylene. The sparsity of peaks in the mass spectra for the mixture indicates that the initial formation and growth of species associated with soot particles are not readily explained by the HACA mechanism.

For indene, the initial mass peaks at *m/z* 216, 228, 230, 330, and 344 are closely linked to reactions involving the indenyl radical. For the ethylene-indene mixture, reactions involving indenyl can also be linked to the mass peaks at *m/z* 178 ($C_{14}H_{10}$), 202 ($C_{16}H_{10}$), 228 ($C_{18}H_{12}$), and 230 ($C_{18}H_{14}$), but the absence of peaks at *m/z*

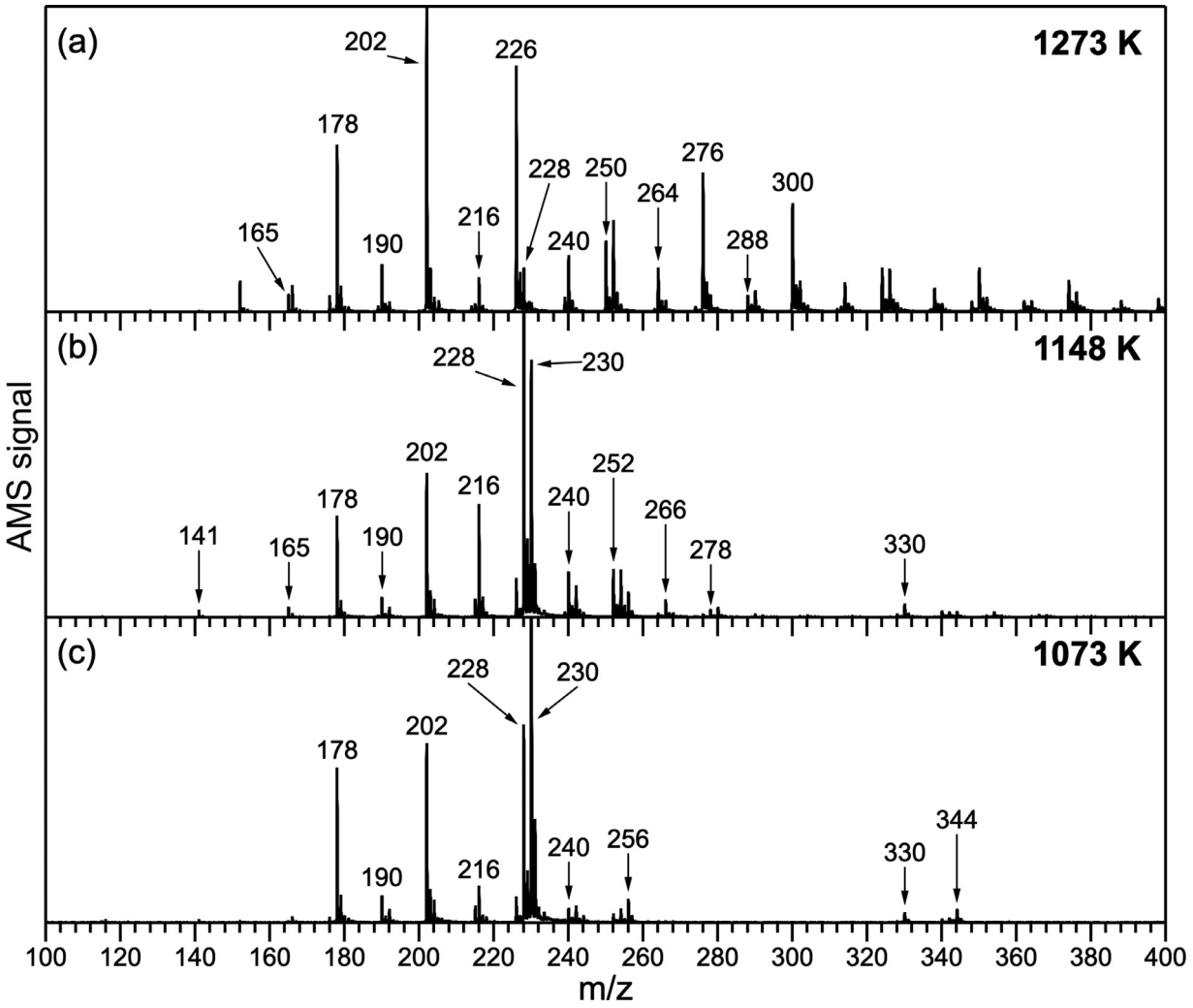

Fig. 5. VUV-AMS mass spectra of ethylene-indene mixture pyrolysis products. Results are shown for reactor temperatures of (a) 1273 K, (b) 1148 K, and (c) 1073 K. The data were recorded with a photon energy of 9.5 eV. Major peaks and masses corresponding to proposed resonance-stabilized radicals and relevant close-shell species are labeled.

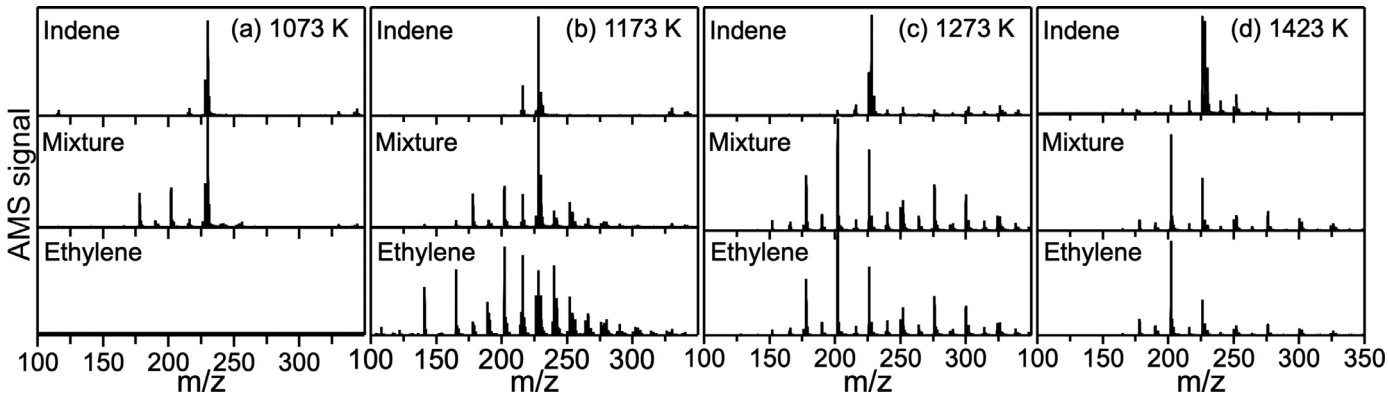

Fig. 6. VUV-AMS mass spectra of pyrolysis products for ethylene, indene, and the ethylene-indene mixture. Results are shown for reactor temperatures of (a) 1073 K, (b) 1173 K, (c) 1273 K, and (d) 1423 K. Data were recorded with a photon energy of 9.5 eV.

178 and 202 in indene pyrolysis indicates that the formation of these masses relies on ethylene or precursors formed in ethylene pyrolysis, which are not available in indene pyrolysis.

Peaks at *m/z* 266 ($C_{21}H_{14}$) and 278 ($C_{22}H_{14}$) are also apparent in the mass spectra for the mixture at temperatures below the onset temperature for ethylene. Species at these masses have been observed to form by non-sequential mass growth in flames, appearing earlier in the soot-formation process than smaller species [37, 68]. Their production appears to skip traditional HACA pathways and instead proceeds through radical-radical reactions [37]. Indene or indenyl apparently facilitates production of these radicals

At higher temperatures, indenyl is predicted to participate in reactions with RSRs generated by ethylene pyrolysis. Sinha et al. [40] performed a series of quantum chemical calculations and proposed a route to pyrene and fluoranthene ($C_{16}H_{10}$) formation via the reaction of indenyl with benzyl radicals (Scheme 4). An effi-

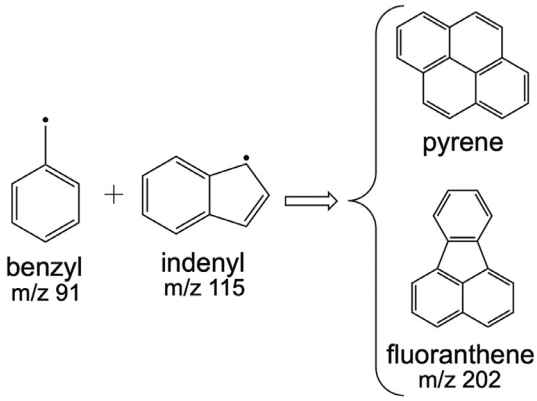

Scheme 4. Summary of pyrene and fluoranthene formation pathways proposed by Sinha et al. [40].

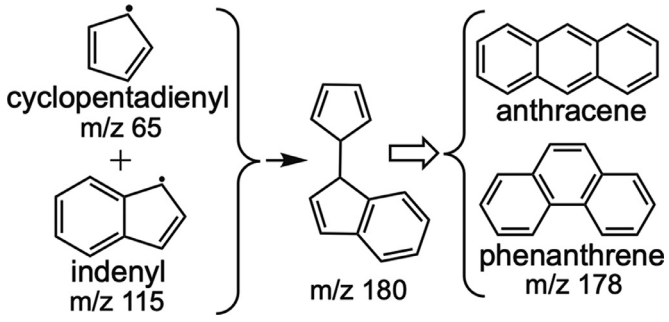

Scheme 5. Summary of anthracene and phenanthrene formation pathways proposed by Mulholland et al. [69].

cient pathway to the formation of anthracene and phenanthrene ($C_{14}H_{10}$) can proceed through the combination of cyclopentadienyl and indenyl radicals [69] (Scheme 5). Whereas both benzyl and cyclopentadienyl radicals may be formed through indene decomposition [48, 70], the availability of these precursors in the ethylene-indene mixture likely relies on their formation via pathways from ethylene pyrolysis.

At temperatures above the onset temperature for ethylene, the presence of mass peaks observed in the mass spectra for ethylene and the ethylene-indene mixture are in excellent agreement for $m/z < \sim 300$. However, the relative intensities of mass peaks are not well matched for these two fuels below 1273 K. The signal intensities for odd-carbon masses are significantly less pronounced relative to the even-carbon species in the ethylene-indene mixture than in ethylene alone, at matching temperatures below 1273 K. This discrepancy may be due to a higher rate of particle inception and precursor growth for the mixture than for ethylene alone; soot inception occurs at a lower temperature for the mixture, which may preferentially partition RSRs in or on particles.

At temperatures of 1273 K and higher, the mass spectra for ethylene and the mixture are nearly identical, as shown in Fig. 6c and d. The apparent tendency of the mixture to behave like ethylene may be expected, given that the relative concentrations of the fuels in the mixture are approximately 98% ethylene and 2% indene by number density, but this behavior is apparent only at high temperatures. At these higher temperatures, the enhanced RSR concentrations offered by small amounts of indene have less of an effect on the flame composition and the distribution of species we sample than at lower temperatures.

3.5. Resonance-stabilized radicals

At temperatures $\leq$1223 K, species growth for both indene and the ethylene-indene mixture appear to be driven primarily by radical-based reactions. Specifically, the indenyl radical is linked to formation pathways for the initial major mass peaks observed for pyrolysis of both indene and the mixture. At intermediate temperatures, between 1223 K and 1373 K, the mass spectra are more densely populated with peak series within the range of *m/z* 150 to 450. These peak series exhibit the typical 24–24–26 u spacing intervals that are consistent with HACA-type growth. The added pool of indenyl radicals does not appear to alter the HACA-based growth of precursors in the ethylene-indene mixture, compared with ethylene at intermediate and higher temperatures, as shown in Fig. 6c and d. At these temperatures indene decomposes, forming acetylene and other smaller hydrocarbons [49].

An increased pool of indenyl radicals in the ethylene-indene mixture is presumably the driving force for decreased onset temperature for the mixture relative to pure ethylene. The indenyl radical facilitates species growth in the mixture, at lower temperatures, by introducing a bicyclic RSR that has efficient pathways for growth through self-reaction or reactions with smaller precursors and other RSRs, such as cyclopentadienyl. The presence of this RSR allows precursors in ethylene pyrolysis to accelerate the particle-inception process.

The influential role of indenyl in precursor growth and soot onset at lower temperatures observed in this study provides clues to the role of RSRs in soot inception. The sparsity of mass peaks and the large separation between peak series near the onset temperature in indene pyrolysis supports the hypothesis that radical reactions, in this case involving indenyl, rapidly grow precursors and initiate inception. This growth pattern agrees with the clustering steps of the CHRCR mechanism, which predicts low barriers for an H-abstraction or H-ejection following a radical-radical reaction.

The first step of the CHRCR mechanism is growth of RSRs through repeated acetylene addition, but the underlying kinetic-thermodynamic coupling in the mechanism does not necessitate a continuous sequence of molecular-weight growth through the addition of acetylene, or other small gas-phase species, to RSRs until they reach a prescribed size. Specific RSR species developed through such addition steps are not mandated and are likely dependent on the fuel and local conditions. The heart of the CHRCR mechanism is the particle-inception process initiated by the pool of RSRs formed. In the CHRCR mechanism, inception occurs through radical-chain reactions that covalently cluster a range of both radical and unsaturated closed-shell hydrocarbon species. In this scheme, clustering refers to the grouping of species that become bound together at growth centers and should not be confused with molecular-weight growth on distributed gas-phase species. Because these reactions are centralized at growth centers, particle inception does not require high concentrations of radicals (e.g., on the order of acetylene concentrations for growth via HACA-type reactions). In addition, the clustering reactions are chain reactions, which regenerate radicals, preventing depletion of the radical pool. The clustering process described by CHRCR is hypothesized to produce disordered, covalently bound, three-dimensional incipient particles.

In the initial stages of the CHRCR mechanism gas-phase precursors may grow through both radical-radical reactions, such as indenyl combinations, and sequential additions of acetylene or vinyl. Reactions between RSRs have previously been projected to provide efficient pathways for mass growth [23, 39, 48, 49, 62, 71]. This behavior is supported by the indenyl-centric growth patterns, observed at low temperatures in both indene and the ethylene-indene mixture, which demonstrate that the progression of RSR

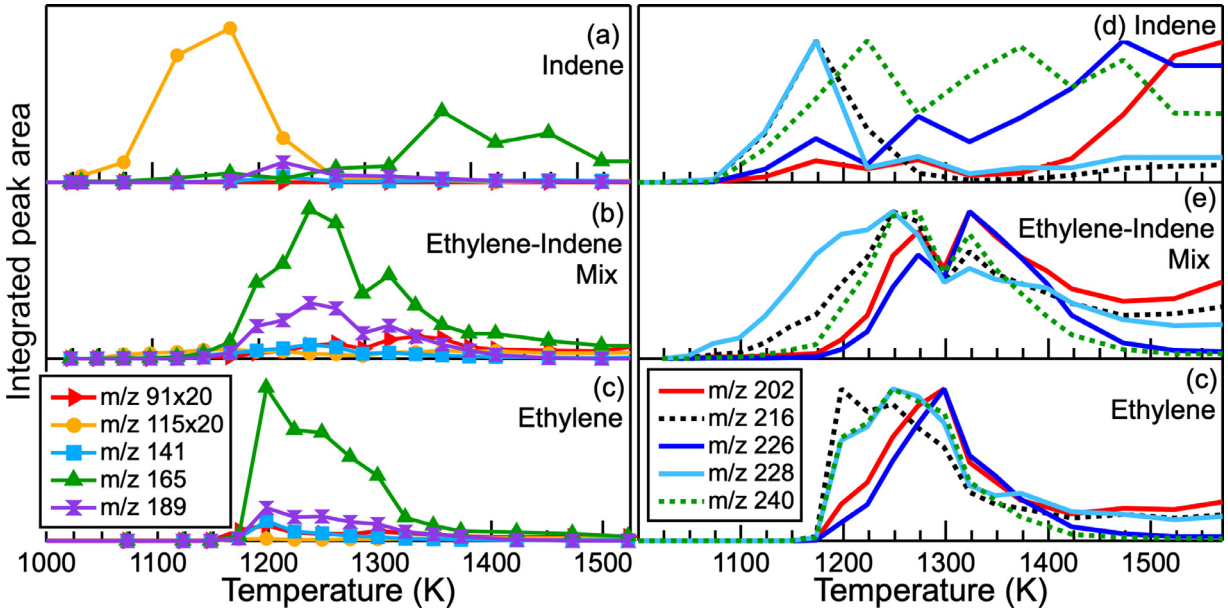

Fig. 7. Temperature dependence of formation of selected masses. Integrated mass peaks are shown for (a-c) masses corresponding to proposed resonance-stabilized radicals and (d-f) selected major peaks corresponding to closed-shell species. The associated fuels are given in the legends. Signals in (a-c) are normalized by the highest peak intensity across all mass peaks for each fuel, and signals in (d-f) are individually normalized by the highest intensity for each mass peak. In (a-c), *m/z* values correspond to molecular formulas of C_7H_7 for *m/z* 91, C_9H_7 for *m/z* 115, $C_{11}H_9$ for *m/z* 141, $C_{13}H_9$ for *m/z* 165, and $C_{15}H_9$ for *m/z* 189. In (d-f), solid lines correspond to even-numbered carbon species ($C_{16}H_{10}$ for *m/z* 202, $C_{18}H_{10}$ for *m/z* 226, and $C_{18}H_{12}$ for *m/z* 228) and dashed lines correspond to odd-numbered carbon species ($C_{17}H_{12}$ for *m/z* 216 and $C_{19}H_{12}$ for *m/z* 240).

growth and clustering is not limited to a strict growth sequence driven by the addition of vinyl or acetylene. Other recent work has also validated pathways and species consistent with this stage of the CHRCR mechanism [32, 72]. This conclusion explains the very early results of Davies and Scully [42] and Graham et al. [43], which showed that the yield of soot from indene was more than an order of magnitude higher than the yield from acetylene at the same concentrations.

Fig. 7a, b, and c present intensity variations with temperature for masses corresponding to RSRs. The most prominent radical masses depend on the fuel. For ethylene (Fig. 7c) and the ethylene-indene mixture (Fig. 7b), the most prominent radical masses are *m/z* 165 and 189, whereas *m/z* 115 and 165 are prominent for indene (Fig. 7a). As expected, the mass peak corresponding to indenyl at *m/z* 115 (scaled up by a factor of 20 in Fig. 7a, b, and c) is more prominent for indene pyrolysis, compared to the other fuels. The trends in Fig. 7a-c illustrate that the importance of individual RSRs, along with the dominant reaction pathways for the formation and growth of specific RSRs, is likely to depend on fuel and reaction conditions.

For both ethylene (Fig. 7c) and the ethylene-indene mixture (Fig. 7b), signal intensities for radicals decrease significantly between 1273 K and 1373 K, whereas the signals for radicals in indene (Fig. 7a) fall off between 1173 K and 1273 K. The temperature range over which radical intensities decrease significantly approximately corresponds to the region with the broadest range of mass peaks. Previous pyrolysis studies on soot particle size and yield have demonstrated that yield and inception rates increase with temperature [46, 47, 73]. PAH sizes, on the other hand, exhibit a maximum before decreasing with further increases in temperature [16, 46, 61]. Continued growth of large PAHs appears to become unfavorable at higher temperatures, resulting in a reduced range of PAH masses. RSR intensities also decrease with increasing temperatures, but this falloff occurs at lower temperatures than those at which PAH growth appears to become unfavorable. This trend suggests that RSRs likely serve as a critical component in the inception process.

Fig. 7d, e, and f demonstrate the relationship between the growth rates of odd-numbered carbon species, corresponding to *m/z* 216 ($C_{17}H_{12}$) and 240 ($C_{19}H_{12}$), and even-numbered carbon species, corresponding to *m/z* 202 ($C_{16}H_{10}$), 226 ($C_{18}H_{10}$), and 228 ($C_{18}H_{12}$). The trends for RSR masses at *m/z* 215 and 239 mirror the trends for the masses at *m/z* 216 and 240 but are omitted for clarity. RSR signals above approximately *m/z* 189 are less prominent, whereas the closed-shell peaks associated with proposed RSR masses within odd-numbered carbon peak series appear with intensities close to or higher than the intensities of the major peaks in adjacent even-numbered carbon peak series. The signal intensities of the odd-numbered carbon species are higher at lower temperatures than the even-numbered carbon species. This observation indicates that the odd-numbered carbon species, and the associated RSRs, which appear in higher concentrations at low temperatures, are closely tied to particle inception.

Odd-carbon species reach their signal maxima 50 – 350 K below the maxima for the even-carbon species. Moreover, the odd-carbon species reach their maxima below 1273 K, which is in the same temperature range in which the RSRs reach their maxima, supporting the association between species with five-membered rings and RSRs [23, 74, 75] and suggesting a role of odd-carbon species in the onset of particle formation. This observation aligns with studies that have linked species containing five-membered rings to soot inception [23, 32, 76-79]. An exception to the trend between odd and even-numbered carbon species is the mass at *m/z* 228, which closely follows the trend of the odd-numbered carbon species. This behavior may result from the close link between *m/z* 228 and indenyl via the reactions between indenyl radicals. If the major pathway to *m/z* 228 is through indenyl reactions, then *m/z* 228 would be expected to mirror the same trends as the RSRs or odd-numbered carbon species. The species associated with *m/z* 226, on the other hand, displays the expected behavior of slower growth with temperature associated with even-numbered carbon. This distinction implies that *m/z* 226 is formed via a different pathway than *m/z* 228, and it is unlikely that *m/z* 226 and *m/z* 228 are related by hydrogen addition/elimination reactions.

The observation that the odd-carbon species reach a peak at lower temperatures than do the even-carbon species is consistent with the even-carbon species being more stable at higher temperatures than the odd-carbon species. We would then expect that particle inception initiated by even-carbon species would be more likely to occur at higher temperatures, The evidence of a second mode in the SMPS size distribution for indene at 1173 K suggests that these high-temperature even-carbon reactions may provide additional pathways for particle growth, rather than inception, because the particle sizes for the second mode (~100 nm) are much larger than expected for incipient particles. This result suggests that, in a flame, soot inception occurs low in the flame at relatively low temperatures, and growth and maturation occur at higher temperatures and higher heights in the flame.

3.6. Photoionization efficiency curves

Identification of large PAHs and radical species is limited by (1) a lack of existing photoionization cross-sections and (2) the presence of numerous isomers with similar ionization energies [37, 55, 80]. Despite this difficulty in identifying large molecular structures through ionization energies, differences in the PIE curves between different isomers can provide qualitative information about major constituents, even if definitive isomer speciation is not possible [80, 81]. Fig. 8 shows selected experimental PIE curves for three pyrolysis cases: ethylene at 1223 K, ethylene-indene mixture at 1223 K, and indene at 1573 K. These PIE curves were recorded at photon energies between 7.5 and 10.2 eV for masses at *m/z* 216 ($C_{17}H_{12}$), 226 ($C_{18}H_{10}$), 228 ($C_{18}H_{12}$), and 230 ($C_{18}H_{10}$).

The PIE curves for pyrolysis products of ethylene and the ethylene-indene mixture are identical to each other within experimental uncertainties at 1223 K, as shown in Fig. 8 and Fig. S1 in the supplementary material. Differences between PIE curves for products of ethylene and indene are most significant for *m/z* 216, 228, and 230 and suggest the formation of different isomers or different distributions of isomers at these masses between the two fuels. The PIE curves at *m/z* 226 (Fig. 8b), on the other hand, appear to be nearly the same for the two fuels. In indene pyrolysis, the masses at *m/z* 216, 228, and 230 are linked to indenyl self-reactions. Lu and Mulholland [62] attribute the $C_{17}H_{12}$ species at *m/z* 216 in indene to benzofluorenes formed as a product of biindenyl, but alternate formation pathways in ethylene may include cyclopentadienyl addition to acenaphthylene or propargyl addition to anthracene. Such pathways are likely to be more pronounced in indenyl pyrolysis.

Fig. 9 shows comparisons of our experimental PIE curves with reference curves for several masses associated with RSRs. For the masses shown, curves for indene and the ethylene-indene mixture are nearly identical to curves for ethylene (see Fig. 8), and we have included only the curves for ethylene for clarity. The lack of agreement between the experimental and reference PIE curves shown in Fig. 9a demonstrates that *m/z* 142 is unlikely to be predominantly attributable to 1-methylnaphthalene. Given that *m/z* 141 is likely to include vinylindenyl, as proposed by Johansson et al. [23] and in Section 3.3 above, we might expect *m/z* 142 to be vinylindene, but we do not have a reference curve for this isomer.

Fig. 9b shows a similar comparison between *m/z* 165 and the reference curves for fluorenyl radical. This mass appears to be a combination of isomers including fluorenyl, which demonstrates good agreement with the experimental PIE curve at the lower photon energies. We would expect *m/z* 165 and 166 to be linked by H-addition/H-loss reactions. Fig. 9c shows a comparison of the PIE curve for *m/z* 166 with several reference curves. A fit based on a linear combination of these reference curves gives excellent agreement with the experimental curve and yields ~88% fluorene, ~8% 2-(prop–1-yn-1-yl)-naphthalene, and ~4% 3H-benz[*e*]indene. This result, suggesting that fluorene is the main contributor to the signal at *m/z* 166, is consistent with the assignment of fluorenyl as a significant isomeric component at *m/z* 165 since loss of a hydrogen atom from fluorene produces fluorenyl.

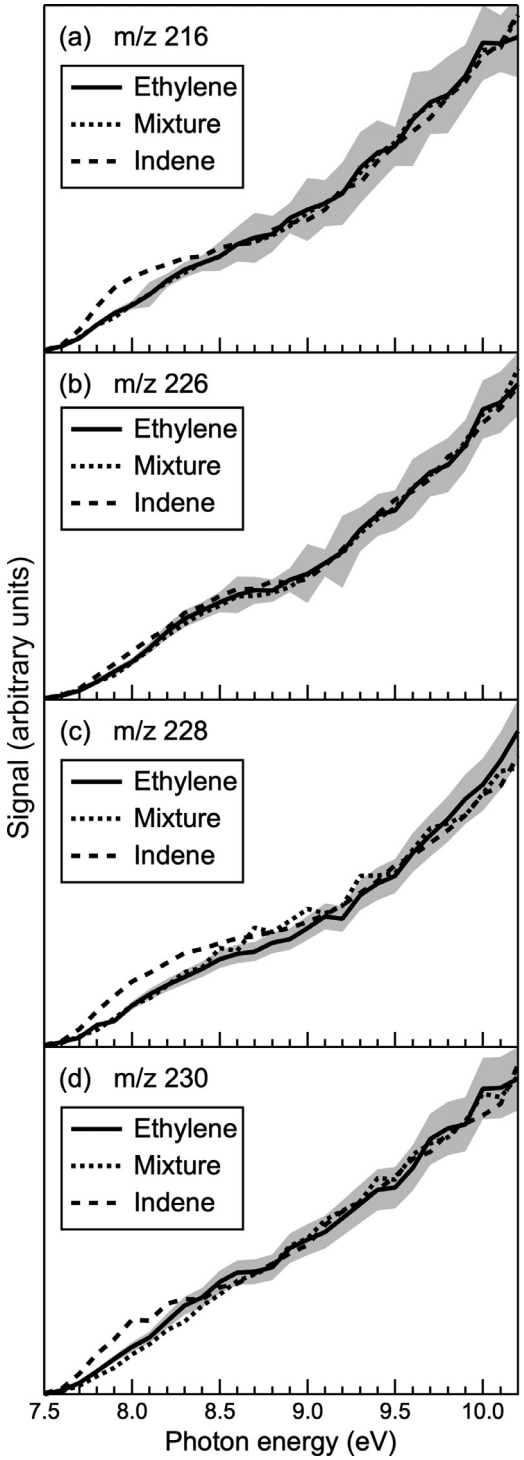

Fig. 8. Normalized photoionization efficiency curves from VUV-AMS data. PIE curves are shown for selected mass peaks for ethylene at 1223 K, the ethylene-indene mixture at 1223 K, and indene at 1573 K. Error bars (gray shading) represent the standard error of the mean.

Zhao et al. [82] suggested a route to forming 3H-benz[*e*]indene (*m/z* 166) through acetylene addition to 1-methylnaphthalene (*m/z* 142). However, the comparisons shown in Fig. 9 demonstrate that *m/z* 142 is unlikely to be predominantly 1-methylnaphthalene, and

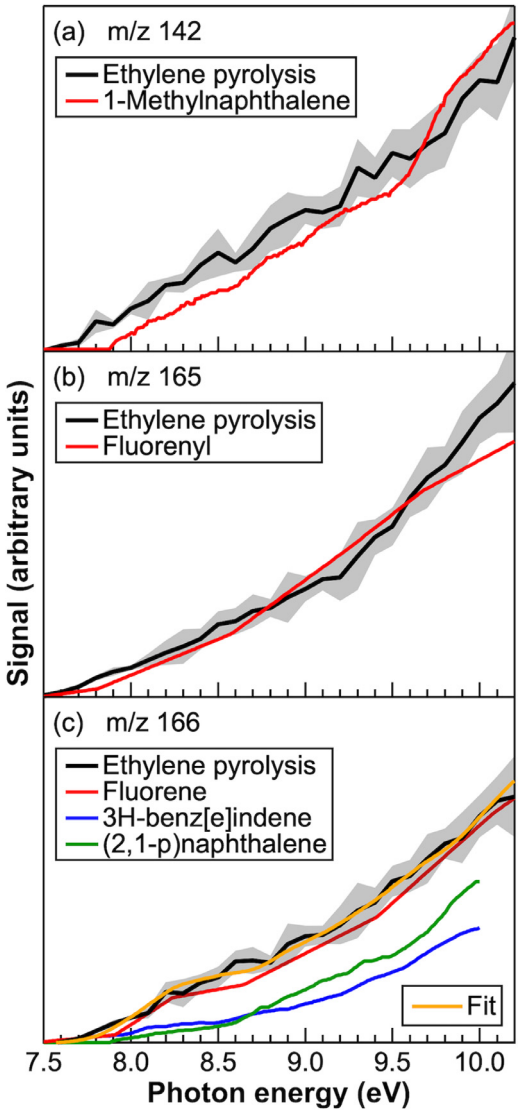

Fig. 9. Normalized photoionization efficiency curves from VUV-AMS data compared to reference PIE curves from the literature. PIE curves are shown for masses associated with resonance-stabilized radicals from ethylene pyrolysis at 1223 K. Error bars (gray shading) represent the standard error of the mean for the pyrolysis data. Reference curves shown are reproduced from [82–84].

m/z 166 is unlikely to be predominantly 3H-benz[*e*]indene, leading us to conclude that acetylene addition to methylnaphthalene is not a major route to forming *m/z* 166 from *m/z* 142.

Table 1 provides a consolidated list of possible assignments for major isomers at selected masses, and Table S1 in Section A of the supplementary material provides a complete list of species for which comparisons were made and the literature sources for all reference curves. Table S2 in the supplementary material presents possible structures for species considered in this study.

Fig. 10 shows a comparison of the PIE curves for other prominent mass peaks in the VUV-AMS data with reference curves available from the literature. Fig. 10 excludes the curves for indene and the mixture for the masses for which those curves are nearly identical to those of ethylene and reference curves for species that were not found to be major contributors to the experimental PIE curve.

PIE curves at *m/z* 202 were compared to reference PIE curves for pyrene and fluoranthene (Fig. 10a). The peak at *m/z* 202 is commonly attributed to pyrene, the most stable isomer at this mass

Table 1
Potential assignments for major isomers produced during pyrolysis.

m/z	Name	Formula	Structure
115	1-Indenyl radical	C_9H_7	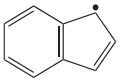
116	Indene	C_9H_8	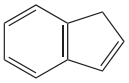
141	Vinylindenyl radical	$C_{11}H_9$	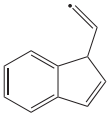
142	Vinylindene	$C_{11}H_{10}$	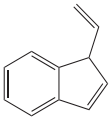
152	Acenaphthylene	$C_{12}H_8$	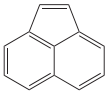
165	Fluorenyl radical	$C_{13}H_9$	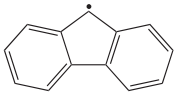
166	Fluorene	$C_{13}H_{10}$	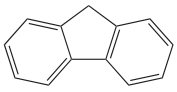
166	3H-benz[*e*]indene	$C_{13}H_{10}$	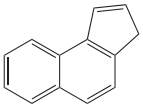
202	Fluoranthene	$C_{16}H_{10}$	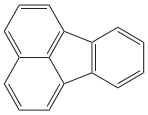
226	Benzo[*ghi*]fluoranthene	$C_{18}H_{10}$	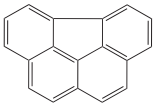
226	7-Ethynylfluoranthene	$C_{18}H_{10}$	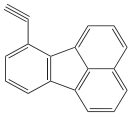
228	Chrysene	$C_{18}H_{12}$	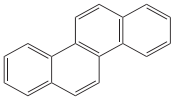
228	4-vinylpyrene	$C_{18}H_{12}$	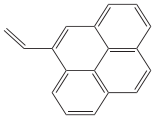
230	1,1-Bi-Indene	$C_{18}H_{14}$	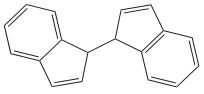

[85], especially in kinetic mechanisms. The fits between the experimental PIE curves and the reference curves indicate that fluoranthene is the primary contributor to *m/z* 202 for ethylene and the ethylene-indene mixture. The PIE curve from indene pyrolysis for *m/z* 202 deviates slightly from both fluoranthene and the curves for ethylene and the mixture. However, a fit using a linear combination of the pyrene and fluoranthene reference curves with scaling and offset parameters did not improve on the fit using fluoran-

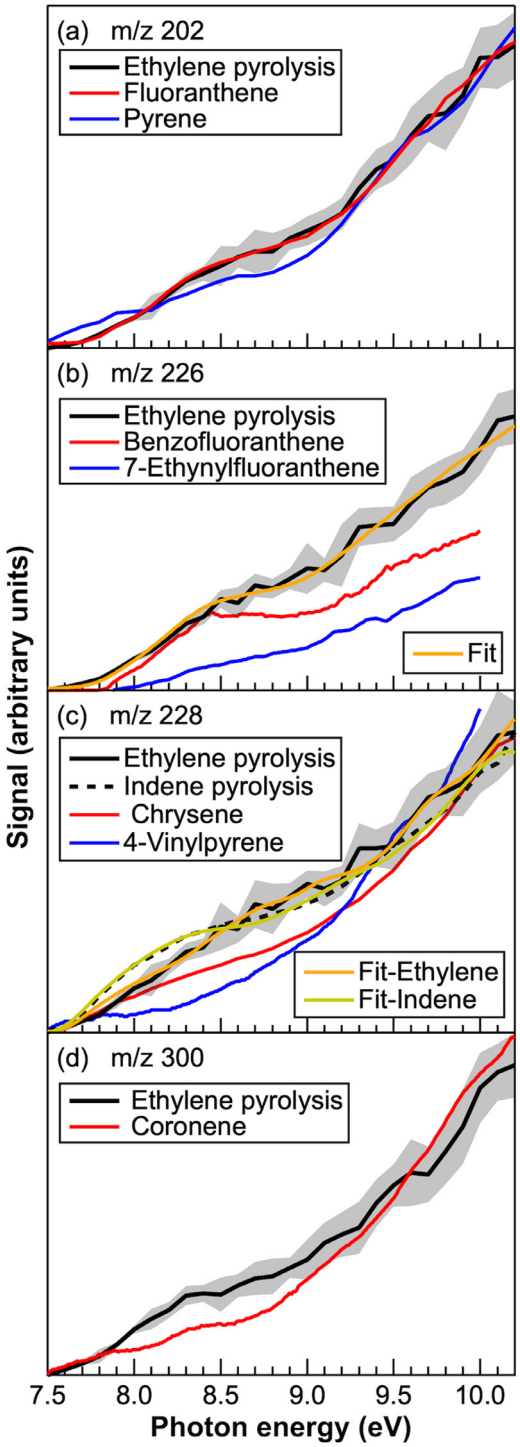

Fig. 10. Normalized photoionization efficiency curves from VUV-AMS data for masses associated with resonance-stabilized radicals compared to reference PIE curves from the literature. PIE curves from VUV-AMS data are shown for ethylene at 1223 K. Error bars represent the standard error of the mean. Reference curves shown are reproduced from [13, 18-20].

thene alone. The result of the combined fit confirms that fluoranthene is a major contributor to the *m/z* 202 peak in the VUV-AMS spectra. This result supports previous studies of the isomeric composition of *m/z* 202 that found the major contribution from isomers other than pyrene and identified fluoranthene as the dominant isomer at this mass [37, 40, 68, 80, 86].

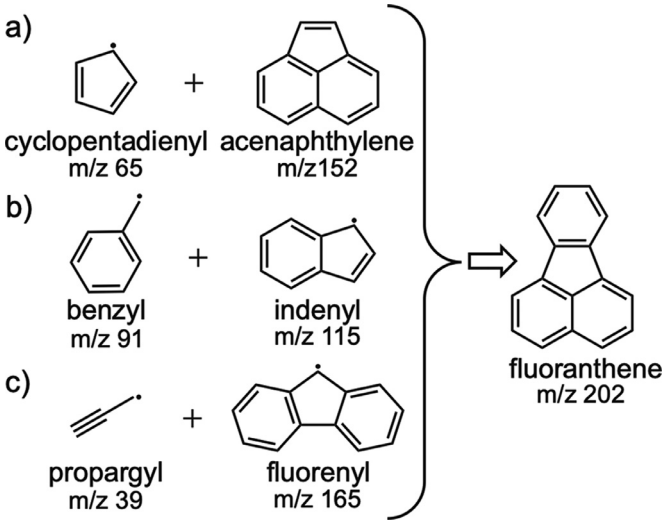

Scheme 6. Summary of fluoranthene formation pathways. Reactions shown were proposed by a) Wang and Violi [87], b) Sinha et al. [40], and c) Jin et al. [48].

There are multiple reaction pathways in the literature that may explain the formation of fluoranthene. Identification of *m/z* 202 as fluoranthene supports proposed growth pathways from acenaphthylene through HACA [17], rather than schemes asserting pyrene formation from phenanthrene as a dominant route. Several pathways for fluoranthene formation have been suggested previously. Wang and Violi [87] proposed fluoranthene formation via cyclopentadienyl addition to acenaphthylene (Scheme 6a); Sinha et al. [40], through the combination of benzyl and indenyl radicals (Scheme 6b), and Jin et al. [48] proposed fluoranthene formation via propargyl addition to fluorenyl (Scheme 6c). These pathways involve reactions of resonance-stabilized radicals with five-membered rings. Notably, a study by Johansson et al. [37] found that pyrene only contributed to 12% of the *m/z* 202 signal from a premixed ethylene/oxygen/nitrogen flame, and the remainder of the signal was due to isomers containing five-membered rings. In a later study, Johansson et al. [80] concluded that *m/z* 202 from this flame was a combination of pyrene and fluoranthene. These observations highlight the limitations of stabilomer reactions and their importance to soot inception [68]. Furthermore, they indicate that five-membered rings play an important role in PAH growth and soot inception, as suggested by other studies [23, 32, 76-79]. Since fluoranthene is the dominant C_{16} species, growth via HACA or radical-based reactions supports previous assignments of benzo[*ghi*]fluoranthene as a prominent $C_{18}H_{10}$ isomer [17].

In contrast to the PIE curves for *m/z* 216, 228, and 230, the curves for ethylene pyrolysis and indene pyrolysis at *m/z* 226 are reasonably consistent with each other. These differences in the comparisons of the PIE curves for *m/z* 226 and 228 support our conclusion, based on differences in temperature dependences of these species, that, despite being close in mass, these species are likely formed via different pathways; *m/z* 226 is not simply the result of hydrogen losses from species at *m/z* 228. The reference curve for benzo[*ghi*]fluoranthene at *m/z* 226 appears reasonably consistent with the experimental PIE curves. However, fits including 7-ethynylfllluoranthene yield better agreement with the experimental curves. The best fit for *m/z* 226 is provided by ~57% from benzo[*ghi*]fluoranthene and ~43% from 7-ethynylfluoranthene.

For *m/z* 228, there are differences between the experimental PIE curves for ethylene and indene pyrolysis, as shown in Fig. 8c; these differences suggest different isomeric compositions at this mass between the two fuels. The mass peak at *m/z* 228 is commonly ascribed to chrysene [14, 16, 48] as it is the stabilomer at this

mass [85]. Our results demonstrate that chrysene is not the sole contributor to the *m/z* 228 peak for ethylene or indene pyrolysis. Other potential isomers of $C_{18}H_{12}$, such as benzo[*c*]phenanthrene and benz[*a*]anthracene, have been proposed for reactions involving the dimerization of indenyl radicals [48]. Fits based on the linear combination of available reference curves demonstrate that a combination of chrysene (~49%), 4-vinylpyrene (~43%), and 9-(but–3-en-1-yn-1-yl)-phenanthrene (~8%) is a consistent representation of the experimental curve for indene pyrolysis, whereas a combination of chrysene (~67%), 4-vinylpyrene (24%), and triphenylene (~9%) produced a reasonable representation of the experimental curve for ethylene pyrolysis.

Finally, we compared experimental PIE curves to a reference curve for coronene (*m/z* 300). The reference curve for coronene was not consistent with the experimental curves for the corresponding masses. Although *m/z* 300 is commonly assumed to be coronene [58, 88], this species was not found to be sole contributors to *m/z* 300 in our experiments. This finding is similar to the conclusion that *m/z* 250 is not predominantly the stabilomer corannulene, as shown in Fig. S2 in the supplementary material. Likewise, the stabilomers anthracene and phenanthrene appear not to be the sole contributors to *m/z* 178, as discussed in Section A.3 of the supplementary material. These results support previous work indicating that species from the stabilomer grid proposed by Stein and Fahr [85] do not adequately capture the variety of species and isomers present in the experimental data [68].

4. Conclusions

We conducted an experimental study of the pyrolysis of ethylene, indene, and an ethylene-indene mixture using VUV-AMS and SMPS. Seeding ethylene with a small amount of indene decreased the particle onset temperature by at least 125 K, compared to ethylene alone. The reduction in particle onset temperature for the ethylene-indene mixture was linked to the increased pool of indenyl radicals, formed by the decomposition of indene. These results further support the presence and involvement of resonance-stabilized radicals and radical-induced hydrocarbon-clustering reactions in precursor-mass growth and particle-inception processes. The results also show that odd-numbered carbon species associated with RSRs appear to be closely tied to particle inception, supporting the association between carbon species with five-membered ring structures and RSRs.

PIE curves indicate that fluoranthene is the major contributor to *m/z* 202, and pyrene is not a significant contributor in ethylene, indene, or the mixture. In addition, *m/z* 152 appears to be composed primarily of acenaphthylene, and *m/z* 226 appears to be predominantly benzo[*ghi*]fluoranthene, but both masses have contributions from other isomers. PIE curves also indicate that the most thermodynamically stable species (stabilomers) at *m/z* 178, 226, 228, 250, and 300 were not the sole contributors to these masses in any of the fuels studied. Differences in PIE curves between ethylene and indene at masses of *m/z* 216, 228, and 230 indicate that there are likely contributions from different isomers for the two fuels because of different fuel-dependent formation pathways for these masses.

Mass growth via the CHRCR mechanism appears to be particularly important during initial particle formation at temperatures below ~1173–1223 K. At temperatures less than ~1173 K, the HACA mechanism appears not to be a significant contributor to particle inception and growth, but it may contribute at higher temperatures. These results add to a growing body of work detailing the importance of radical-chain reactions in particle inception and growth. Accurately understanding and modeling soot formation will require further consideration and investigation of these reactions.

Declaration of Competing Interest

The authors declare that they have no known competing financial interests or personal relationships that could have appeared to influence the work reported in this paper.

Acknowledgments

We are very grateful to Prof. Katharina Kohse-Höinghaus for her extensive scientific contributions to the understanding of combustion chemistry, her service in support of combustion science and engineering, and her strong leadership in this field. We thank G. Barney Ellison for many lively conversations and helpful discussions. HAM, KOJ, PES, and KRW were supported by the Gas Phase Chemical Physics Program in the Chemical Sciences Geosciences and Biosciences Division of the Office of Basic Energy Sciences of the U.S. Department of Energy (DOE). KRW was supported under Contract No. DE-AC02-05CH11231. JAR, CMT, and HAM were supported under a sub-contract from Sandia National Laboratories (FWP 21-022187); JAR and HAM were also supported by the College of Engineering and Applied Sciences at the University of Colorado Boulder. RPB was supported by the Sandia Laboratory Directed Research and Development (LDRD) Program. This research used resources of the Advanced Light Source, which is a DOE Office of Science User Facility under contract no. DE-AC02-05CH11231. Sandia National Laboratories is a multi-mission laboratory managed and operated by National Technology & Engineering Solutions of Sandia, LLC, a wholly owned subsidiary of Honeywell International Inc., for the DOE's National Nuclear Security Administration under contract DE-NA0003525. The views expressed in the article do not necessarily represent the views of the DOE or the United States Government.

Supplementary materials

Supplementary material associated with this article can be found, in the online version, at doi:10.1016/j.combustflame.2021.111942.

References

[1] I.M. Kennedy, The health effects of combustion-generated aerosols, Proc. Combust. Inst. 31 (2007) 2757–2770.
[2] N.A.H. Janssen, G. Hoek, M. Simic-Lawson, P. Fischer, L. van Bree, H. ten Brink, M. Keuken, R.W. Atkinson, H.R. Anderson, B. Brunekreef, F.R. Cassee, Black carbon as an additional indicator of the adverse health effects of airborne particles compared with PM10 and PM2.5, Environ. Health Perspect. 119 (2011) 1691–1699.
[3] C. Hutzler, A. Luch, J.G. Filser, Analysis of carcinogenic polycyclic aromatic hydrocarbons in complex environmental mixtures by LC-APPI-MS/MS, Anal. Chim. Acta 702 (2011) 218–224.
[4] F. Caiazzo, A. Ashok, I.A. Waitz, A.H.I. Yim, S.R.H. Barrett, Air pollution and early deaths in the United States. Part I Quantifyig the impact of major sectors in 2005, Atmos. Environ. 79 (2013) 198–208.
[5] E.J. Highwood, R.P. Kinnersley, When smoke gets in our eyes: the multiple impacts of atmospheric black carbon on climate, air quality, and health, Environ. Int. 32 (2006) 560–566.
[6] T.C. Bond, S.J. Doherty, D.W. Fahey, P.M. Forster, T. Berntsen, B.J. DeAngelo, M.G. Flanner, S. Ghan, B. Kärcher, D. Koch, S. Kinne, Y. Kondo, P.K. Quinn, M.C. Sarofim, M.G. Schultz, M. Schulz, C. Venkataraman, H. Zhang, S. Zhang, N. Bellouin, S.K. Guttikunda, P.K. Hopke, M.Z. Jacobson, J.W. Kaiser, Z. Klimont, U. Lohmann, J.P. Schwarz, D. Shindell, T. Storelvmo, S.G. Warren, C.S. Zender, Bounding the role of black carbon in the climate system: a scientific assessment, J. Geophys. Res. Atmos. 118 (2013) 5380–5552.
[7] Climate Change IPCC, The Physical Science Basis. Working Group I Contribution to the Fifth Assessment Report of the Intergovernmental Panel On Climate Change, Cambridge University Press, Cambridge, UKNew York, NY (2013), p. 2013.
[8] B.S. Haynes, H.G. Wagner, Soot formation, Prog. Energy Combust. Sci. 7 (1981) 229–273.
[9] H.G. Wagner, Soot formation in combustion, Proc. Combust. Inst. 17 (1979) 3–19.
[10] K.-H. Homann, H.G. Wagner, Some new aspects of the mechanism of carbon formation in premixed flames, Proc. Combust. Inst. 11 (1967) 371–379.

[11] M. Frenklach, Reaction mechanism of soot formation in flames, Phys. Chem. Chem. Phys. 4 (2002) 2028–2037.
[12] M. Frenklach, D.W. Clary, W.C. Gardiner Jr, S.E. Stein, Detailed kinetic modeling of soot formation in shock-tube pyrolysis of acetylene, Proc. Combust. Inst. 20 (1985) 887–901.
[13] H. Wang, M. Frenklach, Calculations of rate coefficients for the chemically activated reactions of acetylene with vinylic and aromatic radicals, J. Phys. Chem. 98 (1994) 11465–11489.
[14] H. Wang, M. Frenklach, A detailed kinetic modeling study of aromatics formation in laminar premixed acetylene and ethylene flames, Combust. Flame 110 (1997) 173–221.
[15] J. Appel, H. Bockhorn, M. Frenklach, Kinetic modeling of soot formation with detailed chemistry and physics: laminar premixed flames of C2 hydrocarbons, Combust. Flame 121 (2000) 122–136.
[16] N.E. Sánchez, A. Callejas, Á. Millera, R. Bilbao, M.U. Alzueta, Polycyclic aromatic hydrocarbon (PAH) and soot formation in the pyrolysis of acetylene and ethylene: effect of the reaction temperature, Energy Fuels 26 (2012) 4823–4829.
[17] B. Shukla, M. Koshi, A novel route for PAH growth in HACA based mechanisms, Combust. Flame 159 (2012) 3589–3596.
[18] D.S.N. Parker, R.I. Kaiser, T.P. Troy, M. Ahmed, Hydrogen abstraction/acetylene addition revealed, Angew. Chem. Int. Ed. 53 (2014) 7740–7744.
[19] D.S.N. Parker, R.I. Kaiser, B. Bandyopadhyay, O. Kostko, T.P. Troy, M. Ahmed, Unexpected chemistry from the reaction of naphthyl and acetylene at combustion-like temperatures, Angew. Chem. Int. Ed. 54 (2015) 5421–5424.
[20] T. Yang, T.P. Troy, B. Xu, O. Kostko, M. Ahmed, A.M. Mebel, R.I. Kaiser, Hydrogen-abstraction/acetylene-addition exposed, Angew. Chem. Int. Ed. 55 (2016) 14983–14987.
[21] H. Wang, Formation of nascent soot and other condensed-phase materials in flames, Proc. Combust. Inst. 33 (2011) 41–67.
[22] J.W. Martin, M. Salamanca, M. Kraft, Soot inception: carbonaceous nanoparticle formation in flames, Prog. Energy Combust. Sci. 88 (2022) 100956.
[23] K.O. Johansson, M.P. Head-Gordon, P.E. Schrader, K.R. Wilson, H.A. Michelsen, Resonance-stabilized hydrocarbon radical chain reactions may explain soot inception and growth, Science 361 (2018) 997–1000.
[24] H.A. Michelsen, M.B. Colket, P.-.E. Bengtsson, A. D'Anna, P. Desgroux, B.S. Haynes, J.H. Miller, G.J. Nathan, H. Pitsch, H. Wang, A review of terminology used to describe soot formation and evolution under combustion and pyrolytic conditions, ACS Nano 14 (2020) 12470–12490.
[25] P. Elvati, A. Violi, Thermodynamics of poly-aromatic hydrocarbon clustering and the effects of substituted aliphatic chains, Proc. Combust. Inst. 34 (2013) 1837–1843.
[26] T.S. Totton, A.J. Misquitta, M. Kraft, A quantitative study of the clustering of polycyclic aromatic hydrocarbons at high temperatures, Phys. Chem. Chem. Phys. 14 (2012) 4081–4094.
[27] B.D. Adamson, S.A. Skeen, M. Ahmed, N. Hansen, Nucleation of soot: experimental assessment of the role of polycyclic aromatic hydrocarbons (PAH) dimers, Z. Phys. Chem. (Munich) 234 (2020) 1295–1310.
[28] H. Sabbah, L. Biennier, S.J. Klippenstein, I.R. Sims, B.R. Rowe, Exploring the role of PAHs in the formation of soot: pyrene dimerization, J. Phys. Chem. Lett. 1 (2010) 2962–2967.
[29] P. Elvati, A. Violi, Homo-dimerization of oxygenated polycyclic aromatic hydrocarbons under flame conditions, Fuel 222 (2018) 307–311.
[30] M. Frenklach, H. Wang, Detailed modeling of soot particle nucleation and growth, Proc. Combust. Inst. 23 (1990) 1559–1566.
[31] J.D. Herdman, J.H. Miller, Intermolecular potential calculations for polynuclear aromatic hydrocarbon clusters, J. Phys. Chem. A 112 (2008) 6249–6256.
[32] M. Commodo, K. Kaiser, G. De Falco, P. Minutolo, F. Schulz, A. D'Anna, L. Gross, On the early stages of soot formation: molecular structure elucidation by high--resolution atomic force microscopy, Combust. Flame 205 (2019) 154–164.
[33] A. D'Anna, A. Violi, A. D'Alessio, A.F. Sarofim, A reaction pathway for nanoparticle formation in rich premixed flames, Combust. Flame 127 (2001) 1995–2003.
[34] A. Violi, A. Kubota, T.N. Truong, W.J. Pitz, C.K. Westbrook, A.F. Sarofim, A fully integrated kinetic monte carlo/molecular dynamics approach for the simulation of soot precursor growth, Proc. Combust. Inst. 29 (2002) 2343–2349.
[35] A. Violi, A.F. Sarofim, G.A. Voth, Kinetic Monte Carlo-molecular dynamics approach to model soot inception, Combust. Sci. Technol. 176 (2004) 991–1005.
[36] T. Faravelli, A. Goldaniga, E. Ranzi, The kinetic modeling of soot precursors in ethylene flames, Symposium (International) on Combustion, 27 (1998), pp. 1489–1495.
[37] K.O. Johansson, T. Dillstrom, P. Elvati, M.F. Campbell, P.E. Schrader, D.M. Popolan-Vaida, N.K. Hendersen-Richards, K.R. Wilson, A. Violi, H.A. Michelsen, Radical-radical reactions, pyrene nucleation, and incipient soot formation in combustion, Proc. Combust. Inst. 36 (2017) 799–806.
[38] C.F. Melius, M.E. Colvin, N.M. Marinov, W.J. Pitz, S.M. Senkan, Reaction mechanisms in aromatic hydrocarbon formation involving the C_5H_5 cyclopentadienyl moiety, Symposium (International) on Combustion, 26 (1996), pp. 685–692.
[39] J.A. Miller, S.J. Klippenstein, Y. Georgievskii, L.B. Harding, W.D. Allen, A.C. Simmonett, Reactions between resonance-stabilized radicals: propargyl + Allyl, J. Phys. Chem. A 114 (2010) 4881–4890.
[40] S. Sinha, R.K. Rahman, A. Raj, On the role of resonantely stabilized radicals in polycyclic aromatic hydrocarbon (PAH) formation: pyrene and fluoranthene formation from benzyl-indenyl addition, Phys. Chem. Chem. Phys. 19 (2017) 19262–19278.
[41] M.P. Ruiz, A. Callejas, Á. Millera, M.U. Alzueta, R. Bilbao, Soot formation from C_2H_2 and C_2H_4 pyrolysis at different temperatures, J. Anal. Appl. Pyrolysis 79 (2007) 244–251.
[42] R.A. Davies, D.B. Scully, Carbon formation from aromatic hydrocarbons II, Combust. Flame 10 (1966) 165–170.
[43] S.C. Graham, J.B. Homer, J.L.J. Rosenfeld, The formation and coagulation of soot aerosols generated by the pyrolysis of aromatic hydrocarbons, Proc. R. Soc. Lond. A 344 (1975) 259–285.
[44] Y. Matsukawa, K. Ono, K. Dewa, A. Watanabe, Y. Saito, Y. Matsushita, H. Aoki, K. Era, T. Aoki, T. Yamaguchi, Reaction pathway for nascent soot in ethylene pyrolysis, Combust. Flame 167 (2016) 248–258.
[45] K. Norinaga, O. Deutschmann, N. Saegusa, J.-.I. Hayashi, Analysis of pyrolysis products from light hydrocarbons and kinetic modeling for growth of polycyclic aromatic hydrocarbons with detailed chemistry, J. Anal. Appl. Pyrolysis 86 (2009) 148–160.
[46] K. Dewa, K. Ono, A. Watanabe, K. Takahashi, Y. Matsukawa, Y. Saito, Y. Matsushita, H. Aoki, K. Era, H. Aoki, H. Yamaguchi, Evolution of size distribution and morphology of carbon nanoparticles during ethylene pyrolysis, Combust. Flame 163 (2016) 115–121.
[47] J. Mei, M. Wang, X. You, C.K. Law, Quantitative measurement of particle size distributions of carbonaceous nanoparticles during ethylene pyrolysis in a laminar flow reactor, Combust. Flame 200 (2019) 15–22.
[48] H. Jin, L. Xing, J. Hao, J. Yang, Y. Zhang, C. Cao, Y. Pan, A. Farooq, A chemical kinetic modeling study of indene pyrolysis, Combust. Flame 206 (2019) 1–20.
[49] H. Jin, J. Yang, L. Xing, J. Hao, Y. Zhang, C. Cao, Y. Pan, A. Farooq, An experimental study of indene pyrolysis with synchrotron vacuum ultraviolet photoionization mass spectrometry, Phys. Chem. Chem. Phys. 21 (2019) 5510–5520.
[50] E. Gloaguen, E.R. Mysak, S.R. Leone, M. Ahmed, K.R. Wilson, Investigating the chemical composition of mixed organic-inorganic particles by "soft" vacuum ultraviolet photoionization: the reaction of ozone with anthracene on sodium chloride particles, Int. J. Mass Spectrom. 258 (2006) 74–85.
[51] J. Shu, K.R. Wilson, M. Ahmed, S.R. Leone, Coupling a versatile aerosol apparatus to a synchrotron: vacuum ultraviolet light scattering, photoelectron imaging, and fragment free mass spectrometry, Rev. Sci. Instrum. 77 (2006) 043106.
[52] J.M. Headrick, P.E. Schrader, H.A. Michelsen, Radial-profile and divergence measurements of combustion-generated soot focused by an aerodynamic-lens system, J. Aerosol Sci. 58 (2013) 158–170.
[53] P.S.K. Liu, R. Deng, K.A. Smith, L.R. Williams, J.T. Jayne, M.R. Canagaratna, K. Moore, T.B. Onasch, D.R. Worsnop, T. Deshler, Transmission efficiency of an aerodynamic focusing lens system: comparison of model calculations and laboratory measurements for the Aerodyne Aerosol Mass Spectrometer, Aerosol Sci. Technol. 41 (2007) 721–733.
[54] X. Zhang, K.A. Smith, D.R. Worsnop, J.-.L. Jimenez, J.T. Jayne, C.E. Kolb, J. Morris, P. Davidovits, Numerical characterization of particle beam collimation: part II. Integrated aerodynamic-lens-nozzle system, Aerosol Sci. Technol. 38 (2004) 619–638.
[55] K.O. Johansson, M.F. Campbell, P. Elvati, P.E. Schrader, J. Zádor, N.K. Richards-Henderson, K.R. Wilson, A. Violi, H.A. Michelsen, Photoionization efficiencies of five polycyclic aromatic hydrocarbons, J. Phys. Chem. A 121 (2017) 4447–4454.
[56] WaveMetrics, Igor Pro, Lake Oswego, OR, USA, 2021.
[57] M. Xie, Z. Zhou, Z. Wang, D. Chen, F. Qi, Determination of absolute photoionization cross-sections of oxygenated hydrocarbons, Int. J. Mass Spectrom. 293 (2010) 28–33.
[58] B. Shukla, M. Koshi, Importance of fundamental sp, sp^2, and sp^3 hydrocarbon radicals in the growth of polycyclic aromatic hydrocarbons, Anal. Chem. 84 (2012) 5007–5016.
[59] D.E. Couch, A.J. Zhang, C.A. Taatjes, N. Hansen, Experimental observation of hydrocarbon growth by resonance stabilized radical-radical chain reaction, Angew. Chem. Int. Ed. (2021) in press, DOI: 10.1002/anie.202110929, doi:10.1002/anie.202110929.
[60] L. Zhao, R.I. Kaiser, W. Lu, B. Xu, M. Ahmed, A.N. Morozov, A.M. Mebel, A.H. Howlader, S.F. Wnuk, Molecular mass growth through ring expansion in polycyclic aromatic hydrocarbons via radical-radical reactions, Nat. Commun. 10 (2019) 3689.
[61] O. Mathieu, G. Frache, N. Djebaili-Chaumeix, C.-.E. Paillard, G. Krier, J.-.F. Muller, F. Douce, P. Manuelli, Characterization of adsorbed species on soot formed behind reflected shock waves, Proc. Combust. Inst. 31 (2007) 511–519.
[62] M. Lu, J.A. Mulholland, Aromatic hydrocarbon growth from indene, Chemosphere 42 (2001) 625–633.
[63] G.M. Badger, R.W.L. Kimber, 548. The formation of aromatic hydrocarbons at high temperatures. Part VII. The pyrolysis of indene, J. Chem. Soc. (1960) 2746–2749.
[64] G.M. Badger, S.D. Jolad, T.M. Spotswood, The formation of aromatic hydrocarbons at high temperatures. XXV. The pyrolysis of 3-^{14}C indene, Aust. J. Chem. 19 (1966) 85–93.
[65] C. Wentrup, H.-.W. Winter, D. Kvaskoff, C_9H_8 pyrolysis. *o*-tolylacetylene, indene, 1-indenyl, and biindenyls and the mechanism of indene pyrolysis, J. Phys. Chem. A 119 (2015) 6370–6376.
[66] V.V. Kislov, A.M. Mebel, An ab initio G3-type/statistical theory study of the formation of indene in combustion flames. II. The pathways originating from reactions of cyclic C_5 species-cyclopentadiene and cyclopentadienyl radicals, J. Phys. Chem. A 112 (2008) 700–716.
[67] A. Raj, M.J. Al Rashidi, S.H. Chung, M. Sarathy, PAH growth initiated by propargyl addition: mechanism development and computation kinetics, J. Phys. Chem. A 118 (2014) 2865–2885.

[68] K.O. Johansson, J.Y.W. Lai, S.A. Skeen, D.M. Popolan-Vaida, K.R. Wilson, N. Hansen, A. Violi, H.A. Michelsen, Soot precursor formation and limitations of the stabilomer grid, Proc. Combust. Inst. 35 (2015) 1819–1826.
[69] J.A. Mullholland, M. Lu, D.-.H. Kim, Pyrolytic growth of polycyclic aromatic hydrocarbons by cyclopentadienyl moieties, Proc. Combust. Inst. 28 (2000) 2593–2599.
[70] A. Laskin, A. Lifshitz, Thermal decomposition of indene. Experimental results and kinetic modeling, Symposium (International) on Combustion, 27 (1998), pp. 313–320.
[71] C. Cavallotti, D. Polino, On the kinetics of the $C_5H_5 + C_5H_5$ reaction, Proc. Combust. Inst. 34 (2013) 557–564.
[72] H. Jin, L. Xing, D. Liu, J. Hao, J. Yang, A. Farooq, First aromatic ring formation by the radical-chain reaction of vinylacetylene and propargyl, Combust. Flame 225 (2021) 524–534.
[73] M. Sirignano, A. D'Anna, Coagulation of combustion generated nanoparticles in low and intermediate temperature regimes: an experimental study, Proc. Combust. Inst. 34 (2013) 1877–1884.
[74] F.S. Gentile, F. Picca, G. De Falco, M. Commodo, P. Minutolo, M. Causà, A. D'Anna, Soot inception: a DFT study of σ and π dimerization of resonantly stabilized aromatic radicals, Fuel 279 (2020) 118491.
[75] J.B. Howard, Carbon addition and oxidation reactions in heterogeneous combustion and soot formation, Proc. Combust. Inst. 23 (1990) 1107–1127.
[76] G. da Silva, J.W. Bozzelli, The C_7H_5 fulvenallenyl radical as a combustion intermediate: potential new pathways to the two- and three-ring PAHs, J. Phys. Chem. A 113 (2009) 12045–12048.
[77] S. Fascella, C. Cavallotti, R. Rota, S. Carrà, The peculiar kinetics of the reaction between acetylene and the cyclopentadienyl radical, J. Phys. Chem. A 109 (2005) 7546–7557.
[78] F. Schulz, M. Commodo, K. Kaiser, G. De Falco, P. Minutolo, G. Meyer, A. D'Anna, L. Gross, Insights into incipient soot formation by atomic force microscopy, Proc. Combust. Inst. 37 (2019) 885–892.
[79] G. Vitiello, G. De Falco, F. Picca, M. Commodo, G. D'Errico, P. Minutolo, A. D'Anna, Role of radicals in carbon clustering and soot inception: a combined EPR and Raman spectroscopic study, Combust. Flame 205 (2019) 286–294 .
[80] K.O. Johansson, J. Zádor, P. Elvati, M.F. Campbell, P.E. Schrader, N.K. Richards-Henderson, K.R. Wilson, A. Violi, H.A. Michelsen, Critical assessment of photoionization efficiency measurements for characterization of soot-precursor species, J. Phys. Chem. A 121 (2017) 4475–4485.
[81] L. Zhao, R.I. Kaiser, B. Xu, U. Ablikim, M. Ahmed, M.V. Zagidullin, V.N. Azyazov, A.H. Howlader, S.F. Wnuk, A.M. Mebel, VUV photoionization study of the formation of the simplest polycyclic aromatic hydrocarbon: naphthalene ($C_{10}H_8$), J. Phys. Chem. Lett. 9 (2018) 2620–2626.
[82] L. Zhao, M. Prendergast, R.I. Kaiser, B. Xu, U. Ablikim, W. Lu, M. Ahmed, A.D. Oleinikov, V.N. Azyazov, A.H. Howlader, S.F. Wnuk, A.M. Mebel, How to add a five-membered ring to polycyclic aromatic hydrocarbons (PAHs) - molecular mass growth of the 2-naphthyl radical ($C_{10}H_7$) to benzindenes ($C_{13}H_{10}$) as a case study, Phys. Chem. Chem. Phys. 21 (2019) 16737–16750.
[83] Y. Li, Photoionization Cross Section Database (Version 2.0), National Synchrotron Radiation Laboratory, Hefei, China, 2017.
[84] H. Jin, J. Yang, A. Farooq, Determination of absolute photoionization cross–sections of some aromatic hydrocarbons, Rapid Commun. Mass Spectrom. 34 (2020) e8899.
[85] S.E. Stein, A. Fahr, High-temperature stabilities of hydrocarbons, J. Phys. Chem. 89 (1985) 3714–3725.
[86] T. Mouton, X. Mercier, P. Desgroux, Isomer discrimination of PAHs formed in sooting flames by jet-cooled laser-induced fluorescence: application to the measurement of pyrene and fluoranthene, Appl. Phys. B 122 (2016) 123.
[87] D. Wang, A. Violi, Radical−molecule reactions for aromatic growth: A case study for cyclopentadienyl and acenaphthylene, J. Org. Chem. 71 (2006) 8365–8371.
[88] H. Richter, S. Ganata, W.H. Green, J.B. Howard, Detailed modeling of PAH and soot formation in a laminar premixed benzene/oxygen/argon low-pressure flame, Proc. Combust. Inst. 30 (2005) 1397–1405.